

## Structural mechanisms for VMAT2 inhibition by tetrabenazine

Michael P. Dalton<sup>a</sup>, Mary Hongying Cheng<sup>b</sup>, Ivet Bahar<sup>b</sup>, and Jonathan A. Coleman<sup>a</sup>

*a. Department of Structural Biology, University of Pittsburgh, Pittsburgh, Pennsylvania 15213, USA.*

*b. Laufer Center for Physical and Quantitative Biology, and Department of Biochemistry and Cell Biology, School of Medicine, Stony Brook University, Stony Brook, NY 11794, USA*

Correspondence to Jonathan Coleman: [coleman1@pitt.edu](mailto:coleman1@pitt.edu)

## ABSTRACT

The vesicular monoamine transporter 2 (VMAT2) is a proton-dependent antiporter responsible for loading monoamine neurotransmitters into synaptic vesicles. Dysregulation of VMAT2 can lead to several neuropsychiatric disorders including Parkinson's disease and schizophrenia. Furthermore, drugs such as amphetamine and MDMA are known to act on VMAT2, exemplifying its role in the mechanisms of actions for drugs of abuse. Despite VMAT2's importance, there remains a critical lack of mechanistic understanding, largely driven by a lack of structural information. Here we report a 3.1 Å resolution cryo-EM structure of VMAT2 complexed with tetrabenazine (TBZ), a non-competitive inhibitor used in the treatment of Huntington's chorea. We find TBZ interacts with residues in a central binding site, locking VMAT2 in an occluded conformation and providing a mechanistic basis for non-competitive inhibition. We further identify residues critical for cytosolic and luminal gating, including a cluster of hydrophobic residues which are involved in a luminal gating strategy. Our structure also highlights three distinct polar networks that may determine VMAT2 conformational dynamics and play a role in proton transduction. The structure elucidates mechanisms of VMAT2 inhibition and transport, providing insights into VMAT2 architecture, function, and the design of small-molecule therapeutics.

## MAIN TEXT

### Introduction

Neuronal signaling by monoaminergic neurotransmitters controls all aspects of human autonomic functions and behavior, and dysregulation of this leads to many neuropsychiatric diseases. Nearly 60 years ago<sup>1,2</sup>, secretory vesicles prepared from adrenal glands were shown to contain an activity that accumulated epinephrine, norepinephrine, and serotonin in an ATP-dependent manner<sup>3</sup>. Extensive characterization by many different laboratories of synaptic vesicles (SVs) in neurons showed that monoamine transport activity was also dependent on the proton gradient generated by the V-ATPase, exchanging two protons for one cationic monoamine<sup>4-8</sup>. Monoamine transport was shown to be inhibited by non-competitive inhibitors such as tetrabenazine (TBZ)<sup>9</sup> and competitive inhibitors like reserpine which has been used to treat hypertension<sup>3</sup>. Amphetamines were shown to be monoamine transporter substrates, eventually leading to vesicle deacidification, disruption of dopamine (DA) packaging in the SV, and DA release into the synapse<sup>10</sup>. Cloning of the vesicular monoamine transporter (VMAT) in the 1990's<sup>11-13</sup> revealed two different genes, VMAT1 and VMAT2, that were expressed in the adrenal medulla and brain, respectively<sup>12,14</sup>. VMAT2 is expressed in all monoaminergic neurons in the brain, including those for serotonin, norepinephrine, DA, epinephrine, and histamine<sup>3</sup>, and is essential for loading these neurotransmitters into SVs. VMAT2 is fundamentally required for neurotransmitter recycling and release<sup>15-17</sup> and changes in VMAT1 and VMAT2 activities either through small-molecule agents or mutations are thought to contribute to many human neuropsychiatric disorders including infantile-onset Parkinson's, schizophrenia, alcoholism, autism, and bipolar depression<sup>18-24</sup>.

VMAT1 and 2 are members of the solute carrier 18 (SLC18) family and are also known as SLC18A1 and SLC18A2. The SLC18 subfamily also includes the vesicular transporters for acetylcholine<sup>25</sup> (VACHT, SLC18A3) and polyamines<sup>26</sup> (VPAT, SLC18B1). Sequence alignments

also show that SLC18 transporters belong to the major facilitator superfamily (MFS) of membrane transport proteins which use an alternating access mechanism<sup>27,28</sup> to transport substrate across membranes. SLC18 members are predicted to be comprised of 12 transmembrane (TM) spanning helices (TM1-12), which are arranged in two pseudosymmetric halves each with 6 TM helices containing a primary binding site for neurotransmitters, polyamines, and inhibitors located approximately halfway across the membrane<sup>29</sup> (Fig. 1a). Conformational changes driven by the proton electrochemical gradient are thought to alternatively expose the binding site to either side of the membrane allowing for transport of neurotransmitter from the cytoplasm to the lumen of SVs<sup>30-32</sup>.

VMAT2 and VMAT1 share 62% sequence identity but have distinct substrate specificity and pharmacological properties<sup>33</sup>. Small-molecule ligands such as TBZ and reserpine are high-affinity inhibitors of VMAT2, which prevent neurotransmitters from binding, arrest VMAT2 from cycling, and consequently reduce neuronal signaling. VMAT2 exhibits higher affinity for TBZ, monoamines and amphetamines, whereas reserpine binds equally to both VMAT2 and VMAT1<sup>9</sup>. TBZ is the only drug which is approved for treatment of chorea associated with Huntington's disease and has shown to be effective in various other hyperkinetic conditions such as tardive dyskinesia, dystonia, tics, and Tourette's syndrome<sup>34</sup>. A proposed mechanism for TBZ inhibition of VMAT2 involves two sequential steps, initial low-affinity binding of TBZ to the luminal-open state of VMAT2 which produces a conformational change, resulting in a high-affinity dead-end TBZ-bound occluded complex<sup>30,35-37</sup>.

Here we report a structure of VMAT2 bound to TBZ at 3.1 Å resolution in an occluded conformation using single-particle cryo-electron microscopy (cryo-EM), describing the architecture of VMAT2, identifying the high-affinity TBZ binding site, and revealing the mechanisms of drug and neurotransmitter binding, inhibition, and transport.

## RESULTS

### Cryo-EM imaging of human VMAT2

Since VMAT2 is a small monomeric membrane protein of approximately 55 kDa, cryo-EM structure determination is challenging. To overcome this, we incorporated mVenus and the anti-GFP nanobody into the N- and C-terminus respectively of human VMAT2 to provide mass and molecular features to facilitate the cryo-EM reconstruction (Fig. 1b), this created a hook-like fiducial feature by reconstituting the interaction of these proteins on the cytosolic side of VMAT2<sup>38</sup>. Attachment of both proteins to the termini proved to be ineffective as the unstructured N- and C-terminus of VMAT2 are flexible; to combat this problem, we determined the minimal termini length that would reduce flexibility while maintaining VMAT2 folding. After successive optimizations, our final construct contained mVenus fused to the N-termini at position 17, and the anti-GFP nanobody at position 482 which we denote the VMAT2 chimera (Figure Supplement 1a-e). We investigated the consequences of VMAT2 modification to ensure the chimera maintained functional activity. First, we performed binding experiments with <sup>3</sup>H-labeled dihydrotetrabenazine (DTBZ) and found the chimera bound DTBZ with a similar affinity ( $K_d = 26 \pm 9$  nM) to the wild type control ( $K_d = 18 \pm 4$  nM) (Fig. 1c). Competition binding of labeled DTBZ with unlabeled reserpine which stabilizes cytoplasmic-open<sup>39</sup>, a state which is incompatible with TBZ binding and produced a  $K_i$  of  $173 \pm 1$  nM for reserpine, which was like wild type ( $161 \pm 1$  nM). Next, we performed transport experiments using permeabilized cells, initial time course experiments using <sup>3</sup>H-labeled serotonin showed clear accumulation (Figure Supplement 1f), and steady-state experiments using 1 and 10  $\mu$ M serotonin measured within the linear uptake range showed similar transport activity as wild type VMAT2 (Fig. 1d). Thus, the functional properties of the chimera are comparable to wild type VMAT2.

To understand the architecture, locate the drug binding site, and assess how TBZ binding influences the conformation of the transporter, we studied the VMAT2 chimera using single-particle cryo-EM (Fig. 1e,f, Figure Supplement 2). The resulting cryo-EM map was determined to a resolution of 3.1 Å, the densities of the TM helices were well-defined, continuous, and exhibited density features for TBZ in the primary binding site and most of the side chains (Table 1, Figure Supplement 3). This demonstrates the feasibility of our approach and enabled us to build a model of VMAT2.

### Architecture of VMAT2

The TBZ bound VMAT2 complex adopts an occluded conformation, with TBZ in a binding site between the central transmembrane helices. The twelve TM helices of the transmembrane domain (TMD) of VMAT2 are arranged in a tight bundle with TM1-6 and TM7-12 each organized into a pseudosymmetrical half (Fig. 2a). The cytosolic facing side of VMAT2 is characterized primarily by the unstructured N- and C- termini along with a 20-residue loop that connects the two halves, extending from TM6 to TM7 before terminating in a short  $\alpha$ -helix that runs parallel to the bilayer and connects to TM7 with a short linker. TM5 and 11 both contain proline residues near the luminal face, which break the helical structure and facilitate connections to TM6 and 12 respectively. TM9 and 12 exhibit significant heterogeneity in our cryo-EM reconstructions; we speculate that this is likely due to a dynamic nature intrinsic to the TMs, an aspect that may offer a glimpse into VMAT2 dynamics.

VMAT1 and 2 encode a large luminal loop (LL) 1 which contains several N-linked glycosylation sites<sup>40</sup> and a disulfide bridge between LL1 and LL4<sup>41</sup>. LL1 and 4 also contain intriguing elements of structure: LL1 extends into the luminal space in an unstructured loop which is mostly not resolved in our structure, before terminating in a short helix which interacts with the luminal face of the transporter near TM7, 11 and 12; LL4 extends outward from TM7 into the lumen before connecting back to TM8. A striking feature of LL4 is the location of W318

which positions its indole side chain directly into a luminal cavity near the TBZ site, acting as a plug to completely occlude the luminal side of the transporter (Fig. 2b). Together, these loops cinch the luminal side of the transporter closed, locking VMAT2 in an occluded conformation and preventing ligand egress. The conserved nature of LL4 and W318 suggests this motif is necessary for transport function and is a key player in the transport mechanism (Figure Supplement 1b,g, Figure Supplement 4). The conformation of LL1 and 4 is likely also aided by a disulfide bond between cysteines 117 and 324, which is known to be necessary for transporter function<sup>41</sup>, our structure was not able to unequivocally place this bond due to the lack of density for residues 48-118 of LL1.

### Cytosolic and luminal gates

The structure of the VMAT2-TBZ complex reveals that both the cytosolic and luminal gates are closed, which precludes solvent and ligand access from either the cytosolic or luminal compartments (Fig. 2a-c). Previous studies have suggested residues R217, M221, Y418 and Y422 make up the cytosolic gate<sup>32</sup>. We find R217 and Y418 form the outer cytosolic gate with the guanidino group of R217 involved in a cation-π interaction with the aromatic benzyl group of Y418 which seals off cytosolic access to the binding site (Fig. 2c). M221 and Y422 form a second set of cytosolic gating residues ‘above’ the outer cytoplasmic gate through a stable methionine-aromatic interaction which acts to fully seal the cytoplasmic gate (Fig. 2c). It is likely that M204 and M403 also contribute to cytosolic gating in this region as their side chains also act to fill this space. On the luminal side, F135, F334 and W318, form the luminal gate where they interact with one another to block access to the binding site. W318 acts as ‘cap’ with the indole side chain facing into a tightly packed hydrophobic pocket consisting of residues I44, V131, L134, L315, I317, and I381 which completely prevent access on the luminal side. W318 is highly conserved in the SLC18 family, suggesting that SLC18 transporters share a common mechanism of luminal-gate closure (Figure Supplement 4). E127 of LL1 may play a role in

stabilizing the tryptophan in this conformation, with the carboxyl group of the side chain orienting itself near the indole nitrogen potentially forming a hydrogen bond pair. We found that mutation of this residue to alanine did not significantly reduce TBZ binding relative to wild type (Fig 2d). The inner gate is located just below TBZ and comprises residues Y341, F429, and Y433 (Fig. 2b)<sup>32</sup>. When probed for their role in inhibitor binding, we found that alanine mutants of F135, Y433, and W318 all greatly reduced DTBZ binding (Fig. 2d). Extensive contacts of TBZ with F135 may function to keep the transporter closed on the luminal side, which would trap VMAT2 in the occluded conformation. F135 and Y433 form  $\pi$ -stacking interactions with TBZ which coordinate the benzene ring of TBZ. F429A did not reduce DTBZ affinity ( $K_d = 7.7 \pm 0.6$  nM) compared to the wild type control ( $K_d = 15 \pm 2$  nM), showing that while mutation of this residue compromises the inner cytosolic gate (Fig. 2b), it is not directly involved in binding TBZ. Conversely, while W318 in LL4 also does not interact directly with TBZ, W318 is required for stabilizing the occluded conformation, and replacement with alanine prevents TBZ from being trapped inside the transporter by preventing closure of the luminal gate. Sequence alignment with other members of the SLC18 family reveals broad conservation of W318 except for VACHT which contains a phenylalanine in its place (Figure Supplement 4) and a W318F mutation retained some DTBZ binding ( $K_d = 24 \pm 16$  nM) (Table 2, Fig. 2d). Alignment of VMAT2 sequences from other species also show a high degree of conservation of W318 with some notable exceptions which substitute W318 for a large positively charged residue such as an arginine or histidine; and upon investigation we found these mutants all greatly diminish DTBZ binding (Fig. 2d).

To further investigate the functional role of the identified gating residues, we performed serotonin transport experiments. We found that mutation of both E127, and F135 to alanine significantly reduced transport activity (Fig. 2e). E127A produced a large reduction in transport, resulting in just 34% activity. Replacing F429 with alanine reduced transport as well, but only to

about half the level of wild type (Fig 2e). Interestingly, the Y433A mutation appeared to enhance transport, and while critical for TBZ binding, this mutant does not prevent transporter cycling (Fig. 2d,e). Mutation of W318 to alanine greatly reduced transport, paralleling the effect observed with DTBZ binding (Fig. 2d,e) while a histidine mutant at this position maintained a significant amount of transport activity (Fig. 2d-f) and the phenylalanine substitution had about half the activity of wild type. The highest activity of the examined W318 mutants was W318R, which fully recapitulated the transport activity of wild type despite being unable to bind DTBZ (Fig. 2d, e).

### **Polar networks**

Upon careful inspection of the model, we were able to identify distinct polar networks that we believe may play a role in proton coordination and subsequent transporter conformational change (Fig. 3a). The first and largest of these networks lies between TMs 1, 4 and 11, and consists of residues D33, N34, K138, Q142, R189, Q192, S196, S197, S200 and D426 (Fig. 3b)<sup>31</sup>. At the center of this network lies D33<sup>32</sup>, which makes critical contacts with the side chains of N34, K138, S196, and Q192. Together, the residues comprise a complex hydrogen bond network linking TM 1, 4 and 11. D426<sup>42</sup> lies further toward the cytosol with the side chain carboxyl group facing the bulk of the network, likely forming a hydrogen bond with the hydroxyl group of S200. In the other TMD half there are two distinct groups of interacting polar residues, which bridge between TM 7, 8 and 10 (Fig. 3a,c,d). The second group is a pair of residues found on the luminal side, between residues E312 and N388 with the amide group of the N388 side chain pointed towards the carboxyl group of E312, which could act to stabilize TBZ in the binding site (Fig. 3c). The third group is located toward the cytosolic side and consists of N305, Y341, and D399<sup>42</sup>, the latter two of which have previously been speculated to form a hydrogen bond pair<sup>31</sup>. The side chains of these residues are positioned toward one

another, with the carboxyl group of D399 forming a hydrogen bond with N305 and likely Y314 (Fig 3d).

### **Tetrabenazine binding site**

The resolution of our map allowed us to unambiguously place TBZ in the central binding site (Fig. 4a,b). TBZ adopts a pose which is predominantly perpendicular to the direction of the TM helices in the luminal half of VMAT2 near the location of the luminal gating residues. The TBZ binding site exhibits an amphipathic environment, comprised of both polar and non-polar residues where the tertiary amine of TBZ orients itself towards the negatively charged surface of the binding site near TMs 7 and 11, and toward E312 (Fig. 4c, Figure Supplement 5a). We considered that E312 may play an analogous role to the highly conserved aspartate residue present in neurotransmitter sodium symporters such as the serotonin, DA, and norepinephrine transporters<sup>43</sup> which utilize a negatively charged residue to directly bind to amine groups (Fig. 4d,e Figure Supplement 4). We thus performed radiolabeled binding experiments to assess the effect of mutating residues in the TBZ binding site by measuring binding of <sup>3</sup>H-labeled DTBZ (Fig. 4f, Table 2). E312 was previously shown to be necessary for substrate transport and inhibitor binding, so we first selected this residue for mutagenesis to probe its importance in TBZ binding<sup>31,44</sup>. The E312Q mutant did not fully abolish DTBZ binding (Figure Supplement 5b) but did greatly reduce DTBZ affinity. This demonstrates that, while not completely essential, E312 is important for inhibitor binding and likely substrate transport by interacting with the amine of the neurotransmitter (Fig. 4d,e). Next, we observed that R189 orients its guanidino group towards the methoxy groups of TBZ likely forming hydrogen-bonding interactions and we found that replacement of R189 with an alanine nearly completely abolished DTBZ binding at all concentrations tested (Fig. 4f, Figure Supplement 5b). The high degree of conservation of this residue suggests that it plays an important role in transporter function, and even a conservative substitution to a lysine nearly eliminated DTBZ binding (Fig 4f, Table 2). K138 has been

previously shown to play an important role in both TBZ binding and serotonin transport and the primary amine side chain is positioned toward the TBZ binding site<sup>42</sup> (Fig. 4d,e). K138 is positioned between two aspartate residues (D426 and D33) and is part of a hydrogen bond network that has been previously hypothesized<sup>42</sup>. Previous experiments found that mutating K138 to alanine resulted in an approximate 4-fold reduction in TBZ binding affinity<sup>31</sup> but did not extinguish TBZ binding and therefore K138 is likely involved in direct interactions with substrate or inducing conformational changes during proton transport and is not directly involved in TBZ binding. N34 is of particular interest since the amide group of its sidechain appears to form a hydrogen bond with the carbonyl oxygen of TBZ (Fig 4d,e) and DTBZ binding was not detectable to N34 mutants of either glutamine, threonine or aspartate while substitution to alanine preserved some binding (Fig. 4f, Table 2, Figure Supplement 5b).

To investigate the functional role of residues in the binding site, we again performed a series of serotonin transport experiments. We found R189A, E312Q, N34T, N34A and K138A mutations all exhibited reduced transport activity (Fig. 4g). R189A and E312Q exhibited the largest change, reducing transport to essentially zero. Substitution of N34 with glutamine had little or no effect on transport activity, opposite of what was noted for DTBZ binding. Replacing N34 with alanine was detrimental, reducing transport to less than half of wild type (Fig. 4g). We found N34D and N34T to have opposing effects, with N34D having activity slightly less than wild type and N34T having little to no transport activity at all. R189K greatly affected transport but retained some activity despite lacking measurable DTBZ binding.

Our model of the VMAT2-TBZ complex allowed us to pinpoint two residues which contribute to the specificity of TBZ to VMAT2 over VMAT1. Previous studies have highlighted V232<sup>44</sup>, which is a leucine in VMAT1, as being putatively involved in conferring differences in affinity, and our model shows that V232 is positioned closely to the isobutyl of TBZ which is wedged into a small hydrophobic pocket (Figure Supplement 5c). The addition of an extra

carbon of the leucine sidechain would produce a steric clash and limit the ability of TBZ to bind (Fig. 4e). The V232L mutant in VMAT2 reduces the affinity of DTBZ to VMAT2, confirming its importance in specificity, but the V232L mutant did not show a complete loss in binding (Fig. 4f, Figure Supplement 5b). Therefore, we carefully inspected the binding site of VMAT2 and compared it to the predicted structure of VMAT1 to find additional differences in the binding site (Figure Supplement 4), we found that L37 in VMAT2 is a phenylalanine in VMAT1 (Figure Supplement 5c). Given its proximity to TBZ, this substitution would produce a steric clash with the benzene ring (Figure Supplement 5a,c). We found that the L37F mutant resulted in nearly no detectable binding of DTBZ at 60 nM concentration (Figure Supplement 5b). Thus, the combination of these two substitutions likely constitutes the differences in TBZ affinity of VMAT2 vs. VMAT1. Interestingly, V232L and L37F both retained some transport activity with L37F producing a more significant reduction in activity (Fig 4g).

Our docking simulations suggested that TBZ may sample two different binding poses by small reorientation and movements within the same binding pocket (Figure Supplement 6), both exhibiting similar binding affinities ( $-9.5 \pm 0.2$  kcal/mol); the first pose is almost identical to that resolved in our cryo-EM structure (0.4 Å RMSD, Figure Supplement 6e); and the second (3 Å RMSD in TBZ heavy atom coordinates) shows a reorientation of the TBZ methoxy groups toward C430, a residue previously identified to play an important role in binding TBZ<sup>45</sup> (Figure Supplement 6f). These two poses were also observed in molecular dynamics (MD) simulations as illustrated in Figure Supplement 6.a-d and Movie Supplement 1-4. The second pose provides insights into the adaptability of TBZ to the conformational dynamics of VMAT2, while it preferentially positions itself into the pocket resolved in our cryo-EM map. TBZ is thought to enter from the luminal side of VMAT2 by binding to the luminal-open conformation<sup>37</sup>. It may interact first with C430 and the other coordinating residues at this pose before R189 moves between the two methoxy groups and allows TBZ to settle into the resolved orientation (Figure

Supplement 6f). This result highlights the stepwise events that inhibitors like TBZ may undergo to stably bind to their targets.

The binding stability of TBZ is also influenced by its protonation state. When TBZ is protonated ( $\text{TBZ}^+$ ), it induces the diffusion of 3-4 times more water molecules within the TBZ binding pocket compared to neutral TBZ (Table 3, Figure Supplement 7). This flux of water results in the dissociation of TBZ from its binding site as illustrated in Movie Supplement 5 and 6. Several titratable residues, including D33, E312, D399, D426, K138, and R189, line the central cavity of VMAT2 and impact TBZ binding stability (Table 4). We found that maintaining an overall neutral charge within the TBZ binding pocket, as observed in system TBZ\_1, most effectively preserves the TBZ-bound occluded state of VMAT2. Residues R189 and E312 in particular are within close proximity of TBZ and participate directly in binding.

### **Neurotransmitter release**

To examine the binding propensity of DA to VMAT2 in the occluded conformation, we constructed five simulation systems with varying protonation states for the four acidic residues (D33, E312, D399, and D426) that line the binding pocket (Table 5). For all five systems, DA carried a +1 charge and was initially placed with a pose predicted by docking simulations to be the most favorable binding pose (Figure Supplement 8a,b); and for each system, two MD runs of 100 ns were performed, except for the case where all acidic residues were in a protonated state of which one of the runs was extended to 200 ns to visualize the release of DA to the vesicular lumen. The simulations revealed alterations in DA's binding properties depending on the protonation states of the four acidic residues (Figure Supplement 8c, Table 5). Two notable differences were observed when comparing DA to TBZ binding (system DA\_2 vs. TBZ\_1). First, upon binding TBZ, R189 orients its guanidino group toward the methoxy groups of TBZ and forms hydrogen bonds in both the cryo-EM structure and MD simulations; in the case of DA, hydrogen bond formation of the hydroxyl groups of DA was primarily facilitated by K138, D33 or

D426, or N34, rather than R189. This resulted in the exposure of R189, triggering a continuous water pathway near the hydrophobic gate residue F135 (Fig. 5a). This water path recurred in multiple runs conducted with DA and was lined by the hydrophilic network composed of Y182, R189, Q192, S137, K138, D33, N34, Q142, N146, S200, and D426 (Figure Supplement 8d).

Second, an additional water wire near the hydrophobic gate residue F334 was observed in DA-bound VMAT2 (Fig. 5a), but not in TBZ-bound VMAT2 which, in contrast, was minimally hydrated (Fig. 5b). The second water wire was lined by the backbone polar groups of hydrophobic residues, e.g., F334, together with a hydrophilic network containing K379, N388, S338, E312, Y433, Y341, N305, and D399. We also observed that the amine group of DA acted to facilitate the water influx from the luminal side.

We hypothesize that those two water paths may be related to proton transfer and be associated with protonating the pocket-lining acidic residues. Likely, luminal DA release depends on the number of protonated acidic residues (Figure Supplement 8d-h). When at least two acidic residues were protonated, we observed fluctuations in DA position (run DA\_2; Movie Supplement 7) and dislocation of DA from its pocket (run DA\_3; Movie Supplement 8). In system DA\_4 (Table 5), the protonation of E312, D399, D426, and D33 resulted in complete opening of the hydrophobic gates formed by F135, W318, and F334, which led to the release of DA to the vesicle lumen (Fig. 5c, Movie Supplement 9). DA was observed to migrate toward a cluster of acidic residues, including E127, E120, D121, and D123, before complete dissociation, and the acidic environment within the vesicle lumen should assist in promoting the release of DA.

## DISCUSSION

The VMAT2 – TBZ complex captures the transporter in a fully occluded state with the ligand binding site centrally located between the two repeated substructures TM1-6 and TM7–12. VMAT2 functions by alternating access which involves alternate exposure of the primary

binding site to either side of the membrane and isomerization between a cytosolic-open and luminal-open state in a mechanism known as the rocker-switch (Fig. 6a,b)<sup>3,29,46</sup>. Studies have proposed that TBZ first enters VMAT2 from the luminal side, binding to a luminal-open conformation<sup>35</sup>. TBZ makes extensive contact with residues in the primary site, likely in a lower affinity state as the transporter subsequently closes to forming the high-affinity occluded state. The luminal gates lock the transporter into an occluded state, preventing displacement by other ligands and producing a so-called dead-end complex<sup>32,34,35,47</sup> (Fig. 6a).

Comparison of the transmembrane domain with more distantly related MFS transporters in other conformational states such as the outward-open VGLUT2<sup>48</sup> and inward-open GLUT4<sup>49</sup> models (1.2 Å RMSD) show that the conformational changes involving TM1, 7, 8 and 11 are likely involved in mediating the transport cycle and alternating access (Figure Supplement 10). Comparison with the Alphafold model shows that while the TMD is largely similar (1.1 Å RMSD overall difference in TMD), Alphafold lacks several key features such as the conformations of the LLs and is unable to predict key details that are critical to ligand binding. Hence, computational docking could not identify the TBZ binding site using the Alphafold-predicted model, alluding to the critical importance of our experimental structural data (and simulations based on that structure) for gaining insights into VMAT2 functional mechanisms.

To enable us to solve the structure of VMAT2, we developed an intrinsic fiducial tool consisting of mVenus and the anti-GFP Nb which provides a feature on the cytosolic side of the transporter. GFP and the GFP-Nb are ubiquitous tools used for cell biology, protein biochemistry and structural biology and here we describe another application of this powerful toolkit. In contrast to traditional antibody-based campaigns which may require multiple rounds of screening and take many months or years to discover a suitable binder, our strategy only required us to make between 15-20 constructs to find a suitable chimera (Figure Supplement 1a-c). There are now many other similar methods such as the fusion of the target protein with

BRIL and binding of the anti-BRIL Fab<sup>50</sup> and fusions of maltose-binding protein and DARPin<sup>51</sup>.

However, since our strategy directly incorporates fluorescent proteins, this enables FSEC based screening of constructs and monitoring fluorescence throughout purification<sup>52</sup>. One obvious disadvantage of all intrinsic fiducial strategies is that the fusion may distort the protein structure, but monitoring the functional activity and comparison with the wild type protein should mitigate these problems.

Among human mutations in VMAT2 causing an infantile-onset form of parkinsonism<sup>53–55</sup>, three mutants, P316A, P237H, and P387L, have been shown to extinguish monoamine transport. We find these residues are in LL4 and the luminal ends of TM5 and 9 respectively (Figure Supplement 9). LL4 is involved in luminal gating and the P316A variant would likely disrupt the conformation of the loop. In the case of P237H, a histidine would result in not only an insertion of a positively charged residue into the luminal membrane interface but also in a reduction of the helical bend and would distort the connection of TM5 with TM6. The P387L variant would also disrupt helical connections and the overall architecture of the helix by insertion of a bulky residue into a small hydrophobic cavity. Therefore, we speculate that these SNPs alter the transporter's ability to sample multiple conformations by suppressing transporter dynamics and perturbing VMAT2 stability and folding. Recently, many additional disease variants have been discovered<sup>56</sup> many of which are also found in the luminal or cytoplasmic ends of TM helices, LL1, and the N- and C-termini and our structure will provide insight into the functional and structural consequences of these variants.

Large aromatic side chains of the luminal gating residues compartmentalize the transporter, likely ensuring directional transport of substrate. MD simulations revealed little variation in the pose of the aromatic gating residues comprising the inner gates (Figure Supplement 6d). It is interesting to note that substitution of Y433 with alanine resulted in enhanced transport while reducing DTBZ binding. Reduced inhibitor binding is likely due to

disruption of  $\pi$ -stacking interactions, but the mechanism for enhanced transport remains unclear. The luminal gates showed more movement in MD simulations of DA, likely owing to its residue composition and lack of strong interactions (Fig. 5). Despite this observation, we assert that the tight hydrophobic environment prevents exchange into the luminal space. These mechanisms of gating are atypical of MFS transporters which more commonly use salt bridges to gate access to the substrate binding site<sup>46</sup>.

Of particular interest among gating residues is W318, which acts as a central plug to prevent solvent access to the transporter. Our mutagenesis analysis suggests that while a large residue is required for maintaining some transporter function, lack of charge also appears to be essential for inhibitor binding. Replacement of W318 with residues present in VMAT2 from other species, except for the phenylalanine mutant, failed to recapitulate any DTBZ binding. Interestingly, of these substitutions, only an arginine was able to fully recapitulate native transport, suggesting luminal gating activity requires either a large, charged or a large aromatic residue. Our studies also suggest E127 plays a role in luminal gating by interacting with LL4 as substitution to alanine reduced transport, and we speculate that large, charged groups at position 318 directly interact with E127 to maintain full transporter function. In contrast, DBTZ binding remained unaffected for the E127A mutant, suggesting a role for this residue in a later step of transporter closure of the luminal compartment. Positively charged residues at position 318 may stabilize the luminal gate and promote conformational cycling through enhanced interactions with negatively charged residues such as E127 but may prevent TBZ from entering the luminal pathway of the transporter in any capacity. Conservation of this residue in the SLC18 family suggests that this is a common mechanism for luminal gating. It is unclear what other structural adaptations are present to enable W318 replacement with large positively charged residues in other VMAT2 sequences, but we suspect that the overall architecture of the luminal domain remains similar. We also note that the disulfide bond between LL1 and 4 plays

a critical role in transport<sup>40</sup>, and the disulfide bond may function to restrict the dynamics of this region to allow W318 to occlude the neurotransmitter binding site during transport.

Residues R189 and K138 stand out as critical for drug binding and inhibition and substrate transport. Simulations highlight the role K138 may play in coordinating with the hydroxy group of neurotransmitters and enabling binding at the central site. These results are consistent with previously observed results demonstrating the critical role K138 plays in substrate transport<sup>31,42</sup>. Remarkably, even mutation to lysine at position 189 abolishes DTBZ binding while still retaining a small amount of transport activity, highlighting the specificity of the DTBZ binding site.

Our structure also provides important clues for understanding the chemical specificity and selectivity of TBZ binding, suggesting that the enhanced affinity of DTBZ is due to preferential interaction with N34. DTBZ is a metabolite of TBZ<sup>47</sup> which differs by only a hydroxyl group vs. a double bonded oxygen and binds to VMAT2 with approximately 2-fold higher affinity<sup>56</sup> (Fig. 4a). Our structure suggests that the amide of N34 acts as a hydrogen bond donor for TBZ, and in the case of DTBZ the hydroxyl of the ligand may act as a hydrogen bond donor for the carbonyl oxygen of N34. We hypothesize that this interaction is more favorable for DTBZ, leading to a higher binding affinity. Valbenazine, a TBZ analogue with a valine attached to the oxygen of the hydroxyl group of DTBZ, binds VMAT2 with a  $K_d$  of 150 nM<sup>58</sup>. We hypothesize that N34 does not form a favorable hydrogen bond with the oxygen of valbenazine and that addition of this larger moiety causes steric clashes in the binding site. Mutation of N34 nearly eliminated DTBZ binding, highlighting its importance in coordinating inhibitor binding. We found N34 is also important for transport, but its precise role remains unclear. Strikingly, replacement with glutamine had no effect on transport whereas aspartate had only a small effect. This suggests that N34 is likely involved in substrate coordination but may not be entirely essential. This is confirmed with the N34A substitution which still showed significant transport activity. In

contrast a threonine substitution was greatly detrimental, but we believe this is likely due to larger active site perturbations.

Comparison of the residues involved in TBZ binding in VMAT2 vs. VMAT1 also provides insight into the selectivity of TBZ by demonstrating that key differences in the ligand binding site are likely responsible for the reduction in TBZ binding affinity observed in VMAT1<sup>9</sup>. L37 and V232 are highlighted, and mutation to the equivalent residue in VMAT1, phenylalanine and leucine respectively, eliminated DTBZ binding but only reduced substrate transport. Given these results, we suggest these are the primary residues involved in determining TBZ selectivity for VMAT2 vs. VMAT1. We suspect VMAT1 exhibits structural differences compared with VMAT2 to accommodate the larger residues and maintain functional activity.

Through MD simulations, we gained insights into the effects of the protonation states of TBZ and E312. Protonation of TBZ at the amine resulted in an unstable complex, and a structure markedly different from the state resolved with electron microscopy. This suggests TBZ remains unprotonated when bound to the occluded state, as the protonated form will not remain in complex with VMAT2. We believe there may be other TBZ bound states such as the luminal-open state where TBZ may be protonated. However, in the terminal complex, E312 must remain protonated suggesting that E312 acts as a hydrogen bond donor to stabilize TBZ in the binding site. Our binding and transport studies further confirm this as the mutation of E312 to glutamine greatly reduces serotonin transport and DTBZ binding (Fig 4f, g). Moreover, mutation of E312 to an alanine has long been known to completely negate all TBZ binding and transport activities<sup>30,31,44</sup> again highlighting the requirement of hydrogen bond pairing with TBZ.

We also highlight three key polar networks which may be involved in conformational changes induced by proton binding during the transport cycle and are likely also involved in mediating proton transduction (Fig. 6a). Taken together, we believe these networks play a

critical role in mediating the conformation changes taking place in the transporter upon substrate or inhibitor binding. We hypothesize that the protonation of D33, E312, D399 and D426 would significantly perturb these interactions by breaking crucial hydrogen bond pairs and/or salt bridges, leading to opening of the cytosolic gate. This falls in line with previous work highlighting the role these residues play in transport through a variety of mutagenesis and functional experiments<sup>30,42,44</sup>. Given the known transport stoichiometry of two protons per neurotransmitter, we speculate that two protons may dissociate back into the lumen, perhaps driven by the formation of salt bridges between D33 and K138 or R189 and E312 for example in an cytosol-facing state. The asymmetry between these two networks is also striking, with the first network consisting of TM1, 4 and 11 being substantially larger. This may allow for larger conformational changes on this side and an overall asymmetry in the cytosolic-open state of the transporter. To our knowledge, this is also an atypical feature in MFS proteins<sup>46</sup> and would represent an interesting adaptation upon the rocker-switch mechanism.

Our studies lead us to propose a mechanism by which TBZ inhibits VMAT2 by first entering the transporter from the luminal open state and subsequently trapping it in an occluded state through a two-step mechanism centered around W318, which acts as a central plug to close off the luminal compartment. This provides a basis for non-competitive inhibition as endogenous neurotransmitter is unable to compete for binding from the closed off cytosolic compartment (Fig 6a). Our results also provide insight into transporter function, and we propose a mechanism for substrate release from the central binding site (Fig 6b). The bound substrate coordinates in the binding site predominantly through interactions with E312 and K138. R189 is directed towards the luminal space where it engages with one of two water channels. Water enters through these channels into the transporter, passing F135 and F334 and inducing conformational change. In our simulations, we find intrusion of water to cause W318 to flip out of the central site which enables neurotransmitter to dissociate from the transporter (Fig. 6b).

In summary, we have developed a new fiducial tool incorporating mVenus and the GFP-Nb into the primary sequence of a previously intractable transport protein of great importance to human health. Cryo-EM of VMAT2 allowed us to pinpoint the luminal and cytoplasmic gates, polar networks likely involved in conformational change and proton transduction, and the conformation and binding site of inhibitors. Our structure facilitated the discovery and detailed analysis of many residues involved in these key molecular mechanisms and enabled further extension in our understanding of neurotransmitter transport. Thus, by capturing the VMAT2 bound with TBZ along with subsequent mutagenesis, binding, transport, and computational experiments, our work delivers insights into the transporter's mechanism of function and provides a framework for understanding the structural underpinnings of neurotransmitter release, transport, and inhibition in VMAT2 and other related transport proteins in the MFS family.

## ENDNOTES

### Acknowledgements

This work was funded by the National Institutes of Health (1R01NS134558 to J.A.C., and 1R01GM139297 to I.B). A portion of this research was supported by NIH grant U24GM129547 and performed at the PNCC at OHSU and accessed through EMSL (grid.436923.9), a DOE Office of Science User Facility sponsored by the Office of Biological and Environmental Research. Microscopy at the University of Pittsburgh was supported by National Institutes of Health grants S10 OD025009 and S10 OD019995 (to James F. Conway).

### Author contributions

M.P.D. and J.A.C. designed the project. M.P.D. performed protein purification, cryo-EM analysis, model building, and biochemical analysis. M.P.D., M.H.C., I.B., and J.A.C. wrote the manuscript. M.H.C. and I.B. designed and performed MD simulations. All authors contributed to editing and manuscript preparation.

### Author information

The data that support the findings of this study are available from the corresponding author upon request. The coordinates and associated volumes for the cryo-EM reconstruction of the VMAT2-TBZ data set have been deposited in the Protein Data Bank (PDB) and Electron Microscopy Data Bank (EMDB) under the accession codes 8THR and 41269. The half-maps and masks used for refinement have also been deposited in the EMDB. Simulation trajectories are available upon request. The authors declare no competing interests. Correspondence and requests for materials should be addressed to coleman1@pitt.edu

## FIGURE LEGENDS

**Figure 1. Cryo-EM reconstruction and functional characterization of VMAT2-tetrabenazine complex.** **a**, Predicted structural elements of VMAT2. The neurotransmitter substrate is bound at the central site (yellow, circle) between the two repeats comprised of TM1-6 and 7–12. The red and blue triangles depict the pseudo two-fold symmetric repeats. A disulfide bond (purple line) is predicted between luminal loops LL1 and LL4. The N-linked glycosylation sites in LL1 are shown as red 'Y' shapes. **b**, Intrinsic fiducial strategy involves attachment of mVenus and GFP-Nb to the N- and C-terminus of VMAT2. **c**, Left panel, plots of [<sup>3</sup>H]-DTBZ saturation binding to wild type VMAT2 (black, circles) and chimera (red, squares). Symbols show the mean derived from n=3 technical replicates. Error bars show the s.e.m. Right panel, graphs of competition binding of <sup>3</sup>H-DTBZ with unlabeled reserpine, error bars show the s.e.m. **d**, Plots of transport into vesicles using 1 and 10 µM <sup>3</sup>H-serotonin for wild type VMAT2 (grey bars) and chimera (red bars). The bars show the means and points show the value for each technical replicate. Error bars show the s.e.m. **e, f** Occluded map of VMAT2-tetrabenazine complex (3.1 Å resolution, contour level 0.336). The mVenus and GFP-Nb fiducial is not shown for clarity.

**Figure 2. VMAT2 conformation and residues involved in gating.** **a**, Overall view of the VMAT2-tetrabenazine (TBZ) complex. TBZ is shown in light green sticks with its map density in transparent surface. **b**, Closeup view of luminal gating residues and TBZ, shown in stick representation together with transparent surface representation of their map density. **c**, Cytosolic gating residues, same representation as in **b**. **d**, Binding of DTBZ to various VMAT2 mutants in the luminal and cytosolic gates including wild type (black), W318R (brown), W318H (light green), E127A (purple), W318F (orange), Y433A (forest green), F429A (blue), W318A (red) and F135A (teal). Data were normalized to wild type with error bars denoting standard deviation. **e**, Serotonin transport activity of luminal and cytosolic gating residue mutants. Symbols show the mean derived from n=6 technical replicates with an identical color scheme to

**d.** Asterisks denote statistical significance from wild type, with no significance being denoted with n.s. Data were normalized to wild type transport. Statistics were calculated in Graphpad Prism using a one-way ANOVA with Dunnett's multiple comparison test. Error bars show the standard deviation. **f**, Alignment of five sequential residues of human VMAT2 (two residues on either side of W318) against their counterparts in *Xenopus laevis* (*Xl*), *Helobdella robusta* (*Hr*) and VMAT1, VACHT, and VPAT from humans. The residues which align with W318 in VMAT2 are shown in red.

**Figure 3. Polar networks.** **a**, Overall view showing three distinct polar networks. Polar residues involved in each network and TBZ are shown in sticks. **b**, Cartoon representation showing a zoomed view of polar network 1. **c**, Polar network 2. **d**, Polar network 3.

**Figure 4. Tetrabenazine recognition and binding.** **a**, Chemical structure of tetrabenazine (TBZ). The blue dotted circle indicates the position of the hydroxyl group in DTBZ. **b**, Density associated with TBZ is shown in green transparent surface sharpened with a B-factor of -50 Å<sup>2</sup>. TBZ is shown in sticks fit to the density. **c**, Electrostatic potential of the TBZ binding site. **d, e**, Binding site of TBZ, residues which are involved in binding are shown in sticks. TBZ is shown in light green sticks and the associated density. **f**, Plots of <sup>3</sup>H-DTBZ saturation binding to wild type (black), V232L (pink), R189A (blue), E312Q (forest green), N34D (orange), N34T (light purple), N34A (teal), N34Q (brown) R189K (purple) L37F (red) and K138A (light green). **g**, Serotonin transport activity of mutants in TBZ binding site. Symbols show the mean derived from n=6 technical replicates with an identical color scheme to f. Asterisks denote statistical significance from wild type, with no significance being denoted with n.s. Statistics were calculated in Graphpad Prism using a one-way ANOVA with Dunnett's multiple comparison test. Error bars show the s.e.m.

**Figure 5. Release of dopamine from the occluded binding site to the lumen through the lumen-facing vestibule and concurrent conformational changes in VMAT2.** Comparison of

**a**, DA (yellow sticks) and **b**, TBZ (green sticks) binding to VMAT2, captured by MD simulations.

Two water pathways are observed in the MD simulations of VMAT2 bound to DA (run DA\_2 in Table 5). Water molecules and key residues are shown in sticks. **c**, Positions of dopamine (DA) (yellow van der Waals (VDW) spheres) with respect to hydrophobic gate composed of F135, W318, and F334 (purple VDW spheres), and charged residues lining the binding pocket at t = 0 ns, 30 ns, 100 ns, 170 ns, and 200ns. W318 side chain isomerization plays a critical role in mediating the opening/closure of the hydrophobic gate, accompanied by the reorientation of F135 side chain, permitting a flux of water molecules eventually giving rise to the destabilization and release of DA to the SV lumen by translocating through a hydrated channel. Waters within 10 Å radius from the center of mass (COM) of the hydrophobic gate residues are displayed.

**Figure 6. Mechanism of tetrabenazine inhibition, and the roles of gating residues and polar interactions networks.** **a**, Cartoon depicting substrate transport and tetrabenazine binding to VMAT2. Neurotransmitter (yellow cartoon) binds to the cytosolic open conformation before being released from the transporter in the luminal open state. Tetrabenazine (green cartoon) binds to the luminal-facing state and induces a conformational change to a high-affinity occluded conformation which is the resolved cryo-EM structure reported in this work. The VMAT2 – tetrabenazine complex highlighting significant features including both cytosolic (slashes) and luminal gates (hexagon and pentagon depicting W318), the three polar networks (numbered circles) and relative location of the tetrabenazine binding site (green). **b**, Water penetrating through two pathways is involved in opening the luminal gate. Dopamine is shown in yellow cartoon. **c**, Opening of W318 is associated with neurotransmitter release.

## METHODS

### Key resources table.

Reagent type (species) or resource	Designation	Source or reference	Identifiers	Additional information
Gene ( <i>Homo sapiens</i> )	Human vesicular monoamine transporter 2	Clone ID 40025175	NCBI Reference Sequence: BC108928	Horizon Discovery
Gene ( <i>Lama glama</i> )	Anti-GFP nanobody	Plasmid #49172		Addgene
Cell line ( <i>Homo sapiens</i> )	HEK293S GnTI	ATCC	Cat # ATCC CRL-3022	Used for expression of VMAT2 (PMID: <a href="#">27929454</a> )
Cell line ( <i>Spodoptera frugiperda</i> )	Sf9	ATCC	Cat # ATCC CRL-1711	Used in production of baculovirus for transduction (PMID: <a href="#">27929454</a> )
Transfected construct (human)	pEG BacMam	Gouaux lab		PMID: <a href="#">25299155</a>
Affinity chromatography resin	Strep-Tactin Superflow high capacity resin	Iba life sciences	Cat#2-1208-500	Affinity purification resin
Chemical compound, drug	n-dodecyl-β-D-maltoside	Anatrace	Cat # D310	Detergent
Chemical compound, drug	Cholesteryl Hemisuccinate	Anatrace	Cat # CH210	Lipid
Chemical compound, drug	Reserpine	Sigma	Cat # 83580	Inhibitor
Chemical compound, drug	Dihydrotetrabenazine	Cayman Chemicals	Cat # 27182	Inhibitor
Chemical compound, drug	[ <sup>3</sup> H]5-HT	PerkinElmer	Cat # NET1167250UC	Radiolabeled substrate

Reagent type (species) or resource	Designation	Source or reference	Identifiers	Additional information
Chemical compound, drug	[ <sup>3</sup> H]dihydrotetabenazine	American Radiolabeled Chemicals	Cat # ART 2119	Radiolabeled inhibitor
Chemical compound, drug	Tetrabenazine	Sigma	Cat # T2952	Inhibitor
Chemical compound, detergent	Digitonin	Sigma	Cat # 300410	Detergent
Software, algorithm	Phenix	PMID: <a href="#">22505</a> <a href="#">256</a>	RRID:SCR_014 <a href="#">https://www.phenix-online.org/224</a>	
Software, algorithm	SerialEM	PMID: <a href="#">16182</a> <a href="#">563</a>	RRID:SCR_017 <a href="#">http://bio3d.colorado.edu/SerialEM</a> <a href="#">293</a>	
Software, algorithm	cryoSPARC	PMID: <a href="#">28165</a> <a href="#">473</a>	RRID:SCR_016 <a href="#">https://cryosparc.com/501</a>	
Software, algorithm	RELION	PMID: <a href="#">23000</a> <a href="#">701</a>	RRID:SCR_016 <a href="#">http://www2.mrc-lmb.cam.ac.uk/relion</a> <a href="#">274</a>	
Software, algorithm	UCSF-Chimera	PMID: <a href="#">15264</a> <a href="#">254</a>	RRID:SCR_004 <a href="#">https://www.cgl.ucsf.edu/chimera/097</a>	
Software, algorithm	Coot	PMID: <a href="#">15572</a> <a href="#">765</a>	RRID:SCR_014 <a href="#">https://www2.mrc-lmb.cam.ac.uk/personal/pemsl/ey/coot</a> <a href="#">222</a>	
Software, algorithm	MolProbity	PMID: <a href="#">20057</a> <a href="#">044</a>	RRID:SCR_014 <a href="#">http://molprobity.biochem.duke.edu/</a> <a href="#">226</a>	
Other	R 2/1 200 mesh Au holey carbon grids	Electron Microscopy Sciences	Cat # Q210AR1	Cryo-EM grids
Other	R 1.2/1.3 200 mesh Cu holey carbon grids	Electron Microscopy Sciences	Cat # Q2100CR1.3	Cryo-EM grids
Other	Copper HIS-Tag YSI	PerkinElmer	Cat # RPNQ0096	SPA beads

## Data reporting

No statistical methods were used to predetermine sample size. The experiments were not randomized, and the investigators were not blinded to allocation during experiments and outcome assessment.

## VMAT2 construct design and cloning

Wild type VMAT2 was expressed as a C-terminal eGFP fusion protein containing an 8x His-tag. The VMAT2 chimera consisted of mVenus<sup>59,60</sup> fused to the N-terminus of VMAT2 at amino acid position 17, and the anti-GFP nanobody<sup>38,60</sup> containing both a 10x His-tag and a TwinStrep tag fused to the C-terminus at position 482 by Infusion cloning. Single point mutants were made using PCR starting from wild type VMAT2 C-terminally tagged eGFP construct, and constructs were initially evaluated using FSEC<sup>52</sup>.

## Expression and purification

VMAT2 was expressed in HEK293S GnT<sup>-</sup> cells<sup>61</sup> using baculovirus mediated transduction<sup>62</sup>. Enriched membranes were first isolated by sonication followed by an initial spin at 10,000g followed by a 100,000g spin and subsequent homogenization. Membranes resuspended in 25 mM Tris pH 8.0 and 150 mM NaCl and frozen at -80°C until use. Membranes were thawed and solubilized in 20 mM n-Dodecyl-β-D-maltoside (DDM) and 2.5 mM cholesteryl hemisuccinate (CHS) with 1 mM DTT and 10 μM TBZ for 1 hr before centrifugation at 100,000g. VMAT2 was purified into buffer containing 1 mM DDM, 0.125 mM CHS, 25 mM Tris, 150 mM NaCl, 1 mM DTT, and 1 μM TBZ pH 8.0 using either a NiNTA column which was eluted in the same buffer containing 250 mM imidazole (for the wild type VMAT2 C-terminally tagged eGFP protein) or a StrepTactin column eluted with 5 mM desthiobiotin. Purified VMAT2 was pooled and concentrated using a 100 kDa concentrator (Amicon) before separating by size-exclusion

chromatography on a Superose 6 Increase column in 1 mM DDM, 0.125 mM CHS, 25 mM Tris pH 8.0, 150 mM NaCl, 1 mM DTT, and 1  $\mu$ M TBZ. Peak fractions were pooled, concentrated to 6 mg/ml with a 100 kDa concentrator before addition of 100  $\mu$ M TBZ, and ultracentrifuged at 60,000g prior to cryo-EM grid preparation.

### **Cryo-EM sample preparation and data acquisition**

The VMAT2 chimera (1.5  $\mu$ l) at a concentration of 6 mg/ml was applied to glow discharged Quantifoil holey carbon grids (1.2/1.3 or 2/1 200 mesh copper or gold). Grids were blotted for 4 seconds at 100% humidity, 4°C, with a blot force of 4 using a Vitrobot Mk IV (ThermoFisher) before flash freezing into a 50/50 mixture of liquid propane/ethane cooled to ~170°C with liquid nitrogen. Movies containing 40 frames were recorded on a FEI Titan Krios operating at 300 kV equipped with a Gatan K3 direct electron detector and a Bioquantum energy filter set to a slit width of 20 eV. Images were collected in super-resolution counting mode at a pixel size of 0.647  $\text{\AA}/\text{pixel}$  with defocus ranges from -1 to -2.5  $\mu\text{m}$  with a total dose of 60  $\text{e}/\text{\AA}^2$ . Images were recorded using SerialEM<sup>63</sup>.

### **Image processing**

Micrographs were corrected using Patch Motion Correction and contrast transfer function estimated using Patch CTF in CryoSPARC v4.2<sup>64</sup>. A total of 24,875 micrographs were collected between two datasets recorded on the same microscope. Particles were initially classified by 2D classification in CryoSPARC to generate an ab-initio model for template picking which resulted in ~10 million picks which were extracted at a box size of 384 binned to 128 and classified multiple times using 2D classification and hetero-refinement using a newly generated ab-initio model, an empty detergent ‘decoy’ class, and a junk class containing random density. The resulting approximately 500,000 particles from each dataset were re-extracted at with a box size of 384 binned to 256, refined using non-uniform refinement<sup>65</sup>, and combined before being

subjected to further classification and refinement. The remaining 212K particles were then re-extracted at full box size of 384, refined, and subjected to Bayesian polishing in RELION 3.1<sup>66</sup>. The resulting 3.5 Å map still exhibited significant anisotropy and was subjected to further rounds of 3D classification and refinement in CryoSPARC with a TMD mask to improve features of the peripheral TMs. The final 65,516 particles resulted in a 3.12 Å map that was sharpened in DeepEMhancer<sup>67</sup> using the mask setting and utilizing a mask around the transmembrane domain only.

### **Model building**

The resulting EM map was sufficient for modeling most VMAT2 sidechains in the TMD. The Alphafold2<sup>68</sup> model of VMAT2 was used for initial fitting and was further refined using RosettaCM<sup>69</sup>. After successive rounds of RosettaCM, the model was locally fit using Coot 0.98<sup>70</sup> and Isolde<sup>71</sup> with the majority of the manual rebuilding being done in Isolde. The model was refined in real space using Phenix 1.2<sup>72</sup> and validated by comparing the FSC between the half maps and the refined model.

### **Radioligand binding assays**

Purified VMAT2 (wild type eGFP tagged and VMAT2 chimera) were diluted to 5 nM in 1 mM DDM, 0.125 mM CHS in 20 mM Tris pH 8.0, 150 mM NaCl with 1 mg/ml CuYSi beads (Perkin Elmer). Protein concentration was estimated using FSEC and a standard GFP concentration curve. Protein was then mixed 1:1 to a final protein concentration of 2.5 nM in detergent buffer containing serially diluted <sup>3</sup>H-labeled DTBZ (American Radiolabeled Chemicals) starting at 60 nM final concentration. Counts were then measured using a Microbeta2 scintillation counter in 96 well plates with triplicate measurements<sup>73</sup>. Specific counts were obtained by subtracting values obtained by the addition of 100 µM reserpine. Mutants were

evaluated similarly from cell lysates of transfected cells. Data were fit to a single-site binding equation using Graphpad Prism.

Competition binding experiments were performed at the same protein concentration in the same detergent buffer. 10 nM  $^3$ H-labeled DTBZ was added to buffer and used for nine 1:1 serial dilutions with detergent buffer which initially contained 100  $\mu$ M reserpine (10  $\mu$ M for chimera). Measurements were done in triplicates and fit with a one-site competitive binding equation in Graphpad Prism.

### **Serotonin transport**

Cells transduced overnight were spun down and resuspended in 140 mM KCl, 5 mM MgCl<sub>2</sub>, 50 mM HEPES-KOH pH 7.4 and 0.3 M sucrose. Cells were permeabilized at 30°C for 10 min in the presence of 5 mM MgATP and 0.01% digitonin<sup>32</sup>. Controls additionally included 100  $\mu$ M reserpine. After 10 min, cells were spun down and resuspended in the same buffer containing 2.5 mM MgATP and incubated at 30°C for 10 min. Cells were then mixed 1:1 with buffer containing  $^3$ H-labeled serotonin at a final concentration of 1 or 10  $\mu$ M and incubated at room temperature for 6 min. Transport was stopped by the addition of ice-cold buffer, and the cells were collected on Glass Fiber C filters. The filters were then counted in scintillation fluid. Time course experiments were performed in the same way using 1  $\mu$ M serotonin.

To evaluate mutants, ~ 5 million cells were transfected with 5  $\mu$ g of DNA using Polyjet reagent. 24 hrs after transfection, the cells were harvested into assay buffer containing 130 mM KCl, 5 mM MgCl<sub>2</sub>, 25 mM HEPES-KOH pH 7.4, 1 mM ascorbic acid, 5 mM glucose and washed once with 1 ml of assay buffer. Cells were permeabilized in 500 ul of assay buffer containing 0.001% digitonin and washed once with 1 ml of assay buffer. Next the cells were resuspended, mixed 1:1 with of 0.2  $\mu$ M  $^3$ H-labeled serotonin with 5 mM ATP in assay buffer, and incubated at room temperature for 15 min. In some cases, 12.5  $\mu$ M reserpine was added to the cells along

with  $^3$ H-labeled serotonin for a control. Cells were washed with 2 ml of ice-cold assay buffer and solubilized with 5% Triton-X100 followed by scintillation counting. Mutant expression was assessed with fluorescent microscopy to ensure protein expression levels were comparable.

### **Molecular dynamics simulations**

The initial MD simulation system was prepared using CHARMM-GUI Membrane Builder module<sup>74</sup>. The structure of VMAT2 bound to TBZ was aligned using PPM2.0 webserver<sup>75</sup> and embedded into 1-palmitoyl-2-oleoyl-sn-glycero-3-phosphocholine (POPC) membrane lipids. The pKa values of titratable residues of VMAT2 in the presence or absence of TBZ were calculated using PROPKA 3.5.0<sup>76</sup>; and the computed pKa values for acidic residues and TBZ are listed in Table 4. Of note, D33 and E312, as well as D399 and D426 (yellow highlights in Figure Supplement 8c and bold in Table 4) are in proximity to TBZ; thus, their protonation states may impact substantially TBZ binding. Given that D33 may form a salt bridge with its nearby K138, we assumed it to be deprotonated; and E312 and D399 were assumed to be protonated because of their comparatively higher pKa values. To further assess how the protonation states on TBZ and/or D426 affect the binding propensity of TBZ, we constructed four different simulation systems (see Table 3) with either protonated or deprotonated TBZ and with/without protonation of D426 (in addition to E312 and D399), denoted as systems TBZ\_1 – TBZ\_4. For each system, TIP3P waters and K<sup>+</sup> and Cl<sup>-</sup> ions corresponding to 0.1 M KCl solution were added to build a simulation box of 92 × 92 × 108 Å<sup>3</sup>. The simulated systems contained approximately 86,000 atoms, including VMAT2 and TBZ, 203 POPC molecules, and 17,400 water molecules.

All MD simulations were performed using NAMD<sup>77</sup> (version NAMD\_2.13), following default protocol and parameters implemented in CHARMM-GUI<sup>78</sup>. Briefly, CHARMM36 force fields were adopted for VMAT2, lipids, and water molecules<sup>79,80</sup>. Force field parameters for both protonated (carried +1 charge) and neutral-charged TBZ were obtained from the CHARMM General Force Field for drug-like molecules<sup>81</sup>; and proton was added using Open Babel<sup>82</sup>. Prior

to productive runs, the simulation systems were energy-minimized for 10,000 steps, followed by 2 ns Nosé–Hoover<sup>83,84</sup> constant pressure (1 bar, 310 K; NPT) simulation during which the constraints on the protein backbone were reduced from 10 to 0 kcal/mol. Finally, the unconstrained protein was subjected to 100-180 ns NPT simulations. Periodic boundary conditions were employed in all simulations, and the particle mesh Ewald (PME) method<sup>85</sup> was used for long-range electrostatic interactions with the pair list distance of 16.0 Å. The simulation time step was set to 2 fs with the covalent hydrogen bonds constrained with the SHAKE algorithm<sup>86</sup>. A force-based switching function was used for Lennard-Jones interactions with switching distance set to 10 Å. Langevin dynamics was applied with a piston period of 50 fs and a piston decay of 25 fs as, well as Langevin temperature coupling with a friction coefficient of 1 ps<sup>-1</sup>. For each system, 2-3 independent runs of 100-180 ns were performed (see Table 3). Snapshots from trajectories were recorded every 100 ps for statistical analysis interactions and structural changes.

For DA bound to the occluded VMAT2, we constructed five simulation systems with varying protonation states for the four pocket-lining acidic residues (denoted as runs DA\_0 to DA\_4; see Table 5). In all systems, the DA carried +1 charge and was initially positioned at the top (lowest energy) docking-predicted binding pose (see Figure Supplement 6a,b); and for each system, two runs of 100 ns were performed, following the same simulation protocols described above for TBZ, except for an extended run of 200 ns conducted to visualize the DA release to the SV lumen, which comprised 170 ns conventional MD simulations, followed by 4 ns of enhanced conformation sampling using the adaptive biasing force method<sup>87,88</sup>, and subsequent 30 ns conventional MD simulations.

## Docking simulations

The binding of dopamine, serotonin, and TBZ to the AlphaFold2 modeled VMAT2 conformer (AF-Q05940-F1-model\_v4) and to the present cryo-EM-resolved structure were

simulated using AutoDock Vina<sup>89</sup>. The molecular structures of protonated DA and serotonin were adopted from the previous studies<sup>90,91</sup>. Docking simulations were carried out using a grid with dimensions set to 65 x 65 x 70 Å<sup>3</sup> to encapsulate the entire structure of the transporter. The exhaustiveness of the simulation was set to 50, and the algorithm returned a maximum of 20 ligand binding poses.

### **Computational data analysis**

MD trajectory analysis and visualization were performed using VMD<sup>92</sup>. For each snapshot, the TBZ binding affinity was evaluated using contact-based binding affinity predictor PRODIGY-LIG<sup>93</sup>; and the number of waters within the TBZ binding pocket were assessed by counting the number of oxygen (OH2) atoms within 3.5 Å of TBZ. For RMSD calculations, the C<sup>α</sup> atoms of VMAT2 and the heavy atoms from TBZ were used after alignment of the simulated VAMT2 onto the cryo-EM structure. The binding pockets of VMAT2 were assessed using Essential Site Scanning Analysis (ESSA)<sup>94</sup> and Fpocket<sup>95</sup>, implemented in ProDy 2.0<sup>96</sup>. Sequence conservation of VMAT2 was computed using the ConSurf server with default parameters<sup>97</sup>. Multiple sequence alignment for SLC18 family members was performed using PROMALS3D<sup>98</sup>.

## TABLES

**Table 1. Cryo-EM data collection, refinement and validation statistics.**

	VMAT2-TBZ (EMDB-41269) (PDB 8THR)
<b>Data collection and processing</b>	
Magnification	77,279
Voltage (kV)	300
Electron exposure (e <sup>-</sup> /Å <sup>2</sup> )	60
Defocus range (μm)	-1.0 – -2.5
Pixel size (Å)	0.647
Symmetry imposed	C1
Initial particle images (no.)	~10,000,000
Final particle images (no.)	65516
Map resolution (Å)	3.12
FSC threshold	0.143
Map resolution range (Å)*	6.6 – 2.8
<b>Refinement</b>	
Initial model used (PDB code)	
Model resolution (Å)	3.7
FSC threshold	0.5
Model resolution range (Å)	20.4 – 3.7
Map sharpening <i>B</i> factor (Å <sup>2</sup> )	
Model composition	
Non-hydrogen atoms	2937
Protein residues	389
Ligands	1
<i>B</i> factors (Å <sup>2</sup> )	

Protein	28.99
Ligand	55.22
R.m.s. deviations	
Bond lengths (Å)	0.0004 (0)
Bond angles (°)	0.37 (15)
Validation	
MolProbity score	1.23
Clashscore	4.34
Poor rotamers (%)	0.96
Ramachandran plot	
Favored (%)	98.0
Allowed (%)	2.00
Disallowed (%)	0.00

\*Local resolution range at 0.5 FSC.

**Table 2. Calculated  $K_d$  values of DTBZ for various single point mutants.**

Mutant	$K_d$ (nM)
WT	15 ± 3
N34A	ND
N34D	ND
N34Q	ND
N34T	ND
E127A	15 ± 6
F135A	ND
R189A	ND
V232L	ND
E312Q	ND
W318A	ND
W318F	24 ± 16
W318H	ND
W318R	ND
F429A	7.7 ± 0.6
Y433A	ND

**Table 3. MD simulation systems of VMAT2 in the presence of TBZ, their properties and simulation durations.**

System id	Protonated residues	Bound ligand	Duration (ns)	Waters in binding pocket <sup>a</sup>	RMSD in VMAT2 C <sup>α</sup> -atoms (Å) <sup>b</sup>	RMSD in TBZ heavy atoms (Å) <sup>c</sup>
TBZ_1	E312 and	TBZ	3 x 180	2.8 ± 1.3	2.4 ± 0.3	2.7 ± 0.5
TBZ_2	D399	TBZ <sup>+</sup>	2 x 100	8.1 ± 1.4	2.4 ± 0.4	5.9 ± 1.4
TBZ_3	E312,	TBZ	3 x 100	4.6 ± 1.4	2.7 ± 0.5	3.5 ± 1.3
TBZ_4	D399, and D426	TBZ <sup>+</sup>	2 x 100	14.3 ± 2.4	2.3 ± 0.2	3.7 ± 0.4

<sup>a</sup> number of water molecules within 3.5 Å of TBZ (or TBZ<sup>+</sup>) averaged over multiple MD snapshots;

<sup>b</sup>RMSDs of VMAT2 C<sup>α</sup> atoms from their initial (cryo-EM resolved) positions; <sup>c</sup>RMSD of the heavy atoms of TBZ from their cryo-EM resolved positions. All averages and standard deviations were calculated between 50 to 100 ns portion of the MD trajectories.

**Table 4. pKa calculations performed by ProPKA 3.5.0.**

Residue	pKa with TBZ	pKa without TBZ	Model pKa
<b>D33</b>	5.48	5.43	3.8
D121	4.46	4.46	3.8
D123	4.75	4.75	3.8
D213	3.23	3.23	3.8
D214	4.95	4.95	3.8
D262	6.44	6.44	3.8
D291	4.44	4.44	3.8
<b>D399</b>	7.64	7.56	3.8
D411	2.74	2.74	3.8
<b>D426</b>	6.38	6.35	3.8
D460	8.19	8.07	3.8
E120	3.06	3.06	4.5
E127	4.77	4.77	4.5
E215	4.27	4.27	4.5
E216	3.91	3.91	4.5
E244	4.52	4.52	4.5
E278	4.22	4.22	4.5
<b>E312</b>	6.71	7.46	4.5
E321	4.53	4.53	4.5
K138	9.86	10.04	10.5
R189	9.10	10.02	12.5
<b>TBZ</b>	8.57		10

The cryo-EM structure (with or without TBZ) was used for pKa calculations using ProPKA 3.5.0. Key residues of interest are written in boldface.

**Table 5. MD simulations of VMAT2 in the presence of dopamine and the observed events**

System #	Protonated residues	Duration (ns)	Waters in binding pocket <sup>a</sup>	VMAT2 RMSD <sup>b</sup> from Cryo-EM (Å)	Observed events
DA_0	none	2 × 100	7.7 ± 1.5	2.6 ± 0.2	Salt bridge formation between DA and D399; influx of water into the binding pocket.
DA_1	D399	2 × 100	10.5 ± 2.2	2.2 ± 0.2	Salt bridges formation between DA and E312; influx of water into the binding pocket.
DA_2	E312, D399	2 × 100	8.8 ± 2.1	2.2 ± 0.3	Fluctuations in DA binding pose while remaining within the binding pocket. Formation of two water wires.
DA_3	E312, D399, D426	2 × 100	8.8 ± 2.1	2.5 ± 0.2	Fluctuations in DA binding pose; dislocation of DA from its binding site in one of the two simulations.
DA_4	E312, D399, D426, D33	1 × 100 1 × 200	11.7 ± 2.3	2.6 ± 0.3	Fluctuations in DA binding pose; dislocation and release of DA in the 200 ns run

<sup>a</sup>number of water molecules within 3.5 Å of dopamine averaged over MD snapshots recorded in the time interval 50-100 ns; <sup>b</sup>RMSDs in VMAT2 C<sup>α</sup> atoms positions; all averages and standard deviations refer to the portion 50-100 ns of MD simulations.

## FIGURE SUPPLEMENT LEGENDS

**Figure Supplement 1. Biochemical characterization, construct design, and sequence conservation of VMAT2.** **a**, The mVenus and GFP-Nb was fused the N- and C-terminus of VMAT2 and the length of the termini are varied to find constructs which can be studied by cryo-EM and retain functional activity. **b**, Sequence and secondary structure prediction. The position of the various transmembrane helices are shown and the position of mVenus and GFP-Nb. **c**, Screening of various constructs by FSEC. **d**, The SEC profile of the 17-481 chimera exhibits a single monodisperse peak. **e**, SDS-PAGE gel showing purified VMAT2 chimera which migrates as a ~75 kDa species. **f**, Time course accumulation of serotonin in vesicles using 1  $\mu$ M  $^3$ H-serotonin for wild type (black trace) and chimera (red trace). **g**, VMAT2 colored by sequence variation from different species, using the Consurf server<sup>1</sup>.

**Figure Supplement 2. Cryo-EM data processing of the VMAT2-tetrabenazine complex.** A representative micrograph (defocus -1.3  $\mu$ m) is shown (scale bar equals 80 nm). The workflow depicts the data processing scheme used to reconstruct VMAT2. Two datasets were collected comprising 7,742 and 17,133 micrographs respectively. Movies were corrected for drift using patch motion correction in cryosparc<sup>64</sup> and resultant micrographs were used to estimate defocus and pick particles. Blob picking followed by template picking was utilized to select approximately 5 million particles from each dataset. 2D classification was used to sort particles and the sorted particles were subjected to ab-initio reconstructions to obtain initial reference. Next, all of the particles picks from each dataset were subjected to multiple rounds of heterogeneous classification/refinement with the ab-initio VMAT2 map and two 'decoy' classes (yellow, a spherical blob and red, empty detergent micelle) starting with a box size of 128 pixels, followed by subsequent rounds of classification at box size of 256. This resulted in approximately 212k particles after combining both datasets. Particles were then extracted at full box size 384 before Bayesian polishing in Relion<sup>66</sup> and local CTF refinement in Cryosparc<sup>64</sup>. The resulting 3.5  $\text{\AA}$  map

was then subjected to Cryosparc 3D classification using a transmembrane domain (TMD) mask<sup>64</sup>. The final stack of 65k particles was then subjected to local refinement to produce the final unsharpened map. DeepEMhancer was used to locally sharpen the map for interpretation<sup>67</sup>.

**Figure Supplement 3. Cryo-EM maps and interpretation of VMAT2 reconstruction.** **a**, Cryo-EM density colored by local resolution estimation. **b**, FSC curves for cross-validation, the unmasked map (blue), loose mask (green), tight mask (red) and the reported corrected (purple) curves. The dotted line indicates an FSC value of 0.143. **c**, FSC curves for model versus half map 1 (working, red), half map 2 (free, blue) and model versus final map (black). **d**, Angular distribution of particles used in the final reconstruction. **e**, Cryo-EM density segments of TM1 to TM12.

**Figure Supplement 4. Sequence alignment of VMAT1, VMAT2, VACChT, and VPAT.** The positions of mutated residues are shown in red boxes. The human variants are shown in blue boxes<sup>97,98</sup>.

**Figure Supplement 5. Point mutants in tetrabenazine binding site.** **a**, 2D cartoon of the TBZ binding site showing only highlighted residues. Green, red, and blue indicate hydrophobic, negative, or positively charged properties of the side chains<sup>99</sup>. **b**, Plots of binding of 60 nM of [<sup>3</sup>H]-DTBZ. The bars show the means and points show the value for each technical replicate. Error bars show the s.e.m. **c**, Binding site showing the positions of L37 and V232 which are a phenylalanine and a leucine in VMAT1 respectively.

**Figure Supplement 6. Tetrabenazine docking and molecular dynamics (MD) simulations.** **a-c**, Time evolution of **a**, root-mean-square-deviations (RMSDs) in VMAT2 C<sup>α</sup> coordinates from those resolved in the cryo-EM structure, **b**, RMSD for TBZ heavy atoms, and **c**, TBZ binding affinities, observed in three different runs conducted for the TBZ\_1 system (see Table 3).

Binding affinities were calculated using PRODIGY-LIG. **d**, The TBZ binding poses and variations of W318 captured in these MD simulations, with a snapshot taken every 4 ns and a total of 50 frames are shown from 0 to 100 ns for each run. The ligand conformations are shown in cyan sticks with blue stick illustrating cryo-EM resolved binding pose. The variations of W318 are displayed in purple sticks with dark purple showing the cryo-EM-resolved orientation. Docking simulations of TBZ onto VMAT2 revealed two poses, shown in the panels **e** and **f**. The former, captured in runs 1 and 3, is almost identical (RMSD of 0.4 Å) to the cryo-EM resolved pose, illustrated in panel **e**. The latter, captured in run 2, differs from the cryo-EM pose by 3.0 Å.

**Figure Supplement 7. Effects of protonation states of TBZ and selected VMAT2 residues on the time evolution of TBZ (heavy atoms) and VMAT2 ( $\alpha$ -carbons) RMSDs from their original (cryo-EM resolved) positions.** Results are presented for three different types of simulations (TBZ\_2 – TBZ-4; see Table 3). In each case, the top panels (**a**, **c**, and **e**) display the RMSDs in the heavy atoms of TBZ and the lower panels (**b**, **d**, and **f**) display the RMSDs in the  $\text{C}^\alpha$ -atoms of VMAT2. Multiple runs are displayed by curves in different colors.

**Figure Supplement 8. Comparisons of binding poses of substrate (DA and serotonin) and inhibitor (TBZ) from docking simulations and MD simulations under different protonation states of substrate-coordinating and/or gating residues.** **a**, Docking of dopamine and **b**, serotonin to the cryo-EM-resolved VMAT2. The most energetically favorable poses are shown for both substrates. Residues within 4 Å of the ligand are shown in sticks. Dopamine and serotonin are displayed in violet and cyan as van der Waals (vdW) surfaces. In both cases, the amine group (of either substrate) is in close contact with E312 and the hydroxyl group interacts with R189. **c**, Resolved 3D positions of aspartates and glutamates in VMAT2. **d**, DA binding pose to the cryo-EM resolved VMAT2 conformer (initial). **e - h**, DA binding poses captured by 100 ns MD simulations of system DA\_0 **f**, in which none of the four acidic residues D33, E312, D399 and D426 were protonated and DA bound to D399; DA\_1 **g**, in which D399 was

protonated and DA bound to E312; DA\_2 (i), in which E312 and D399 were protonated; and DA\_3 h, in which E312, D399, and D426 were protonated. DA is shown in yellow vdW spheres around 100 ns, along with hydrophobic gate residues F135, W318 and F334 (purple vdW spheres), and charged residues lining the binding pocket. Waters within 10 Å radius from the center of mass (COM) of the hydrophobic gate residues are displayed.

**Figure Supplement 9. Human variants of VMAT2.** P316A, P237H and P387L localize to LL4 and the luminal ends of TM5 and TM9, respectively.

**Figure Supplement 10. Comparison of the VMAT2-TBZ structure with the predicted Alphafold structure and with other MFS transporters.** **a**, Comparison of the cryo-EM structure (light blue) vs. Alphafold (navy). The position of TM1, 2, 4, 7, 8, 10, and 11 and LL4 in the cryo-EM structure show the most substantial differences and are shown in white for clarity. **b**, Comparison with the outward-open VGLUT2 structure (PDB: 8SBE) shown in navy. **c**, Comparison with the inward-open GLUT4 structure (PDB: 7WSM) shown in navy.

## Movie Supplement Legends

**Movie Supplement 1** (related to Figure Supplement 6): [Movie\\_S1.mpg](#). Binding and coordination of neutral TBZ (*cyan* van der Waals (vdW) representation observed in a 180 ns MD simulation (*run 1*). Three runs were performed for VMAT2 embedded in a lipid bilayer in the presence of TBZ, where E312 and D399 were protonated. We focus here on the time evolution of TBZ coordination, hence the naming of the runs as TBZ\_1 run 1, TBZ\_1 run 2, and TBZ\_1 run 3. Movie S1 displays TBZ\_1 run 1. For each snapshot, water molecules (in CPK format; ball and stick) within 4 Å of TBZ are shown; and acidic, basic, hydrophilic, and hydrophobic residues within 4 Å of TBZ are displayed in *red*, *blue*, *green* and *orange* *licorice* representations, respectively. The predominant pose adopted by TBZ is closely similar to that resolved in our cryo-EM structure, and illustrated in Figure Supplement 6 panel e. See Table 3 for the description of the runs.

**Movie Supplement 2** (related to Figure Supplement 6): [Movie\\_S2.mpg](#). Binding and coordination of neutral TBZ (*cyan* vdW representation) observed in a 180 ns MD simulation (TBZ\_1 run 2), in the same format as Movie Supplement 1. TBZ slightly altered its position within the same binding pocket, to stabilize the pose illustrated in Extended Data Figure 6 panel f.

**Movie Supplement 3** (related to Figure Supplement 6): [Movie\\_S3.mpg](#). Binding and coordination of neutral TBZ (*cyan* van Der Waals (vdW) format) observed in a 180 ns MD simulation (TBZ\_1 run 3), in the same format as Movie S1. TBZ adopts a pose similar to that resolved in the cryo-EM structure.

**Movie Supplement 4** (related to Table 3): [Movie\\_S4.mpg](#). Same as Movie Supplement 1-3, with neutral TBZ, but with the additional protonation of D426 (TBZ\_3 run1). TBZ adopted the predominant pose similar to that resolved in the cryo-EM structure.

**Movie Supplement 5** (related to Table 3): [Movie\\_S5.mpg](#). MD simulation of the binding and coordination of protonated TBZ ( $\text{TBZ}^+$ ; *pink* vdW format) to VMAT2 with protonated E312 and D399. This is a 100 ns run, termed TBZ\_2 run 1. The same format as Movie Supplement 1-3 is adopted for the coordinating residues. TBZ tends to alter its binding pose to approximate the one observed in Movie Supplement 2.

**Movie Supplement 6** (related to Table 3): [Movie\\_S6.mpg](#). Same as Movie Supplement 4, except for the protonation of TBZ ( $\text{TBZ}^+$  shown in pink vdW representation). This is a 100 ns run, termed TBZ\_4 run 1. In the presence of protonation, TBZ preferentially samples the pose observed in Movie Supplement 2 and 5.

**Movie Supplement 7** (related to Table 5): [Movie\\_S7.mpg](#). Fluctuations in dopamine binding pose (DA; *yellow* vdW spheres) within its binding pocket, observed in a 100 ns MD simulation of VMAT2 in the presence of DA (system DA\_2 in Table 5). VMAT2 E312 and D399 are protonated; and D33 and D426 are deprotonated. Hydrophobic gate residues F135, W318 and F334 are displayed in *purple* vdW spheres, and acidic and basic residues K138 and R189 are shown in *red* and *blue* vdW representation.

**Movie Supplement 8** (related to Table 5: [Movie\\_S8.mpg](#). Release of dopamine (DA; *yellow* vdW spheres) from the binding pocket, observed in a 100 ns MD simulation (system DA\_3 in Table 4). E312, D399 and D426 were protonated and D33 was deprotonated.

**Movie Supplement 9** (related to Figure 5): [Movie\\_S9.mpg](#). Release of DA to the vesicular lumen (*yellow* VDW spheres), observed after protonating D33, E312, D399 and D426 (*red* vdW spheres). The movie represents a 200 ns MD simulation of system DA\_4 in Table 5.

## REFERENCES

1. Carlsson, A., Lindqvist, M. & Magnusson, T. 3,4-Dihydroxyphenylalanine and 5-hydroxytryptophan as reserpine antagonists. *Nature* **180**, 1200 (1957).
2. Kirshner, N. Uptake of catecholamines by a particulate fraction of the adrenal medulla. *J Biol Chem* **237**, 2311–7 (1962).
3. Eiden, L. E. & Weihe, E. VMAT2: a dynamic regulator of brain monoaminergic neuronal function interacting with drugs of abuse. *Ann N Acad Sci* **1216**, 86–98 (2011).
4. Henry, J. P., Sagne, C., Bedet, C. & Gasnier, B. The vesicular monoamine transporter: from chromaffin granule to brain. *Neurochem Int* **32**, 227–46 (1998).
5. Eiden, L. E. The vesicular neurotransmitter transporters: current perspectives and future prospects. *FASEB J* **14**, 2396–400 (2000).
6. Johnson, R. G., Jr. Accumulation of biological amines into chromaffin granules: a model for hormone and neurotransmitter transport. *Physiol Rev* **68**, 232–307 (1988).
7. Eiden, L. E., Schafer, M. K., Weihe, E. & Schutz, B. The vesicular amine transporter family (SLC18): amine/proton antiporters required for vesicular accumulation and regulated exocytotic secretion of monoamines and acetylcholine. *Pflugers Arch* **447**, 636–40 (2004).
8. Schuldiner, S., Shirvan, A. & Linial, M. Vesicular neurotransmitter transporters: from bacteria to humans. *Physiol Rev* **75**, 369–92 (1995).
9. Peter, D., Jimenez, J., Liu, Y., Kim, J. & Edwards, R. H. The chromaffin granule and synaptic vesicle amine transporters differ in substrate recognition and sensitivity to inhibitors. *J Biol Chem* **269**, 7231–7 (1994).
10. Freyberg, Z. *et al.* Mechanisms of amphetamine action illuminated through optical monitoring of dopamine synaptic vesicles in Drosophila brain. *Nat Commun* **7**, 10652 (2016).
11. Liu, Y. *et al.* A cDNA that suppresses MPP+ toxicity encodes a vesicular amine transporter. *Cell* **70**, 539–51 (1992).

12. Peter, D. *et al.* Differential expression of two vesicular monoamine transporters. *J Neurosci* **15**, 6179–88 (1995).
13. Erickson, J. D., Eiden, L. E. & Hoffman, B. J. Expression cloning of a reserpine-sensitive vesicular monoamine transporter. *Proc Natl Acad Sci U A* **89**, 10993–7 (1992).
14. Weihe, E., Schafer, M. K., Erickson, J. D. & Eiden, L. E. Localization of vesicular monoamine transporter isoforms (VMAT1 and VMAT2) to endocrine cells and neurons in rat. *J Mol Neurosci* **5**, 149–64 (1994).
15. Wang, Y. M. *et al.* Knockout of the vesicular monoamine transporter 2 gene results in neonatal death and supersensitivity to cocaine and amphetamine. *Neuron* **19**, 1285–96 (1997).
16. Takahashi, N. *et al.* VMAT2 knockout mice: heterozygotes display reduced amphetamine-conditioned reward, enhanced amphetamine locomotion, and enhanced MPTP toxicity. *Proc Natl Acad Sci U A* **94**, 9938–43 (1997).
17. Fon, E. A. *et al.* Vesicular transport regulates monoamine storage and release but is not essential for amphetamine action. *Neuron* **19**, 1271–83 (1997).
18. Lohoff, F. W. *et al.* Variations in the vesicular monoamine transporter 1 gene (VMAT1/SLC18A1) are associated with bipolar disorder. *Neuropsychopharmacology* **31**, 2739–47 (2006).
19. Vaht, M., Kiive, E., Veidebaum, T. & Harro, J. A Functional Vesicular Monoamine Transporter 1 (VMAT1) Gene Variant Is Associated with Affect and the Prevalence of Anxiety, Affective, and Alcohol Use Disorders in a Longitudinal Population-Representative Birth Cohort Study. *Int J Neuropsychopharmacol* **19**, (2016).
20. Fehr, C. *et al.* Association of VMAT2 gene polymorphisms with alcohol dependence. *J Neural Transm Vienna* **120**, 1161–9 (2013).
21. Bohnen, N. I. *et al.* Positron emission tomography of monoaminergic vesicular binding in aging and Parkinson disease. *J Cereb Blood Flow Metab* **26**, 1198–212 (2006).

22. Han, H. *et al.* The Gene Polymorphism of VMAT2 Is Associated with Risk of Schizophrenia in Male Han Chinese. *Psychiatry Investig* **17**, 1073–1078 (2020).
23. Simons, C. J., van Winkel, R., & Group. Intermediate phenotype analysis of patients, unaffected siblings, and healthy controls identifies VMAT2 as a candidate gene for psychotic disorder and neurocognition. *Schizophr Bull* **39**, 848–56 (2013).
24. Lohoff, F. W. *et al.* Association between polymorphisms in the vesicular monoamine transporter 1 gene (VMAT1/SLC18A1) on chromosome 8p and schizophrenia. *Neuropsychobiology* **57**, 55–60 (2008).
25. Arvidsson, U., Riedl, M., Elde, R. & Meister, B. Vesicular acetylcholine transporter (VACHT) protein: a novel and unique marker for cholinergic neurons in the central and peripheral nervous systems. *J Comp Neurol* **378**, 454–67 (1997).
26. Hiasa, M. *et al.* Identification of a mammalian vesicular polyamine transporter. *Sci Rep* **4**, 6836 (2014).
27. Jardetzky, O. Simple allosteric model for membrane pumps. *Nature* **211**, 969–70 (1966).
28. Mitchell, P. A general theory of membrane transport from studies of bacteria. *Nature* **180**, 134–6 (1957).
29. Radestock, S. & Forrest, L. R. The alternating-access mechanism of MFS transporters arises from inverted-topology repeats. *J Mol Biol* **407**, 698–715 (2011).
30. Yaffe, D., Forrest, L. R. & Schuldiner, S. The ins and outs of vesicular monoamine transporters. *J Gen Physiol* **150**, 671–682 (2018).
31. Yaffe, D., Radestock, S., Shuster, Y., Forrest, L. R. & Schuldiner, S. Identification of molecular hinge points mediating alternating access in the vesicular monoamine transporter VMAT2. *Proc Natl Acad Sci U A* **110**, E1332-41 (2013).
32. Yaffe, D., Vergara-Jaque, A., Forrest, L. R. & Schuldiner, S. Emulating proton-induced conformational changes in the vesicular monoamine transporter VMAT2 by mutagenesis. *Proc Natl Acad Sci U A* **113**, E7390–E7398 (2016).

33. Erickson, J. D., Schafer, M. K., Bonner, T. I., Eiden, L. E. & Weihe, E. Distinct pharmacological properties and distribution in neurons and endocrine cells of two isoforms of the human vesicular monoamine transporter. *Proc Natl Acad Sci U A* **93**, 5166–71 (1996).
34. Kaur, N., Kumar, P., Jamwal, S., Deshmukh, R. & Gauttam, V. Tetrabenazine: Spotlight on Drug Review. *Ann Neurosci* **23**, 176–185 (2016).
35. Scherman, D., Jaudon, P. & Henry, J. P. Characterization of the monoamine carrier of chromaffin granule membrane by binding of [2-3H]dihydrotetrabenazine. *Proc Natl Acad Sci U A* **80**, 584–8 (1983).
36. Scherman, D. & Henry, J. P. Reserpine binding to bovine chromaffin granule membranes. Characterization and comparison with dihydrotetrabenazine binding. *Mol Pharmacol* **25**, 113–22 (1984).
37. Ugolev, Y., Segal, T., Yaffe, D., Gros, Y. & Schuldiner, S. Identification of conformationally sensitive residues essential for inhibition of vesicular monoamine transport by the noncompetitive inhibitor tetrabenazine. *J Biol Chem* **288**, 32160–32171 (2013).
38. Kubala, M. H., Kovtun, O., Alexandrov, K. & Collins, B. M. Structural and thermodynamic analysis of the GFP:GFP-nanobody complex. *Protein Sci* **19**, 2389–401 (2010).
39. Yaffe, D., Forrest, L. R. & Schuldiner, S. The ins and outs of vesicular monoamine transporters. *J Gen Physiol* **150**, 671–682 (2018).
40. Yao, J. & Hersh, L. B. The vesicular monoamine transporter 2 contains trafficking signals in both its N-glycosylation and C-terminal domains. *J Neurochem* **100**, 1387–96 (2007).
41. Thiriot, D. S., Sievert, M. K. & Ruoho, A. E. Identification of human vesicle monoamine transporter (VMAT2) luminal cysteines that form an intramolecular disulfide bond. *Biochemistry* **41**, 6346–53 (2002).
42. Merickel, A., Kaback, H. R. & Edwards, R. H. Charged Residues in Transmembrane Domains II and XI of a Vesicular Monoamine Transporter Form a Charge Pair That Promotes High Affinity Substrate Recognition. *J. Biol. Chem.* **272**, 5403–5408 (1997).

43. Yamashita, A., Singh, S. K., Kawate, T., Jin, Y. & Gouaux, E. Crystal structure of a bacterial homologue of Na<sup>+</sup>/Cl<sup>-</sup>-dependent neurotransmitter transporters. *Nature* **437**, 215–223 (2005).
44. Stove, S. I., Skjevik, A. A., Teigen, K. & Martinez, A. Inhibition of VMAT2 by beta2-adrenergic agonists, antagonists, and the atypical antipsychotic ziprasidone. *Commun Biol* **5**, 1283 (2022).
45. Thiriot, D. S. & Ruoho, A. E. Mutagenesis and derivatization of human vesicle monoamine transporter 2 (VMAT2) cysteines identifies transporter domains involved in tetrabenazine binding and substrate transport. *J Biol Chem* **276**, 27304–15 (2001).
46. Drew, D., North, R. A., Nagarathinam, K. & Tanabe, M. Structures and General Transport Mechanisms by the Major Facilitator Superfamily (MFS). *Chem Rev* **121**, 5289–5335 (2021).
47. Chen, J. J., Ondo, W. G., Dashtipour, K. & Swope, D. M. Tetrabenazine for the treatment of hyperkinetic movement disorders: a review of the literature. *Clin Ther* **34**, 1487–504 (2012).
48. Li, F. *et al.* Ion transport and regulation in a synaptic vesicle glutamate transporter. *Science* **368**, 893–897 (2020).
49. Yuan, Y. *et al.* Cryo-EM structure of human glucose transporter GLUT4. *Nat Commun* **13**, 2671 (2022).
50. Mukherjee, S. *et al.* Synthetic antibodies against BRIL as universal fiducial marks for single-particle cryoEM structure determination of membrane proteins. *Nat. Commun.* **11**, 1598 (2020).
51. Chen, H. *et al.* Structural and functional insights into Spns2-mediated transport of sphingosine-1-phosphate. *Cell* **186**, 2644-2655.e16 (2023).
52. Hattori, M., Hibbs, R. E. & Gouaux, E. A fluorescence-detection size-exclusion chromatography-based thermostability assay for membrane protein precrystallization screening. *Structure* **20**, 1293–9 (2012).

53. Jacobsen, J. C. *et al.* Brain dopamine-serotonin vesicular transport disease presenting as a severe infantile hypotonic parkinsonian disorder. *J. Inherit. Metab. Dis.* **39**, 305–308 (2016).
54. Rilstone, J. J., Alkhater, R. A. & Minassian, B. A. Brain Dopamine–Serotonin Vesicular Transport Disease and Its Treatment. *N. Engl. J. Med.* **368**, 543–550 (2013).
55. Padmakumar, M. *et al.* A novel missense variant in *SLC18A2* causes recessive brain monoamine vesicular transport disease and absent serotonin in platelets. *JIMD Rep.* **47**, 9–16 (2019).
56. Saida, K. *et al.* Brain monoamine vesicular transport disease caused by homozygous *SLC18A2* variants: A study in 42 affected individuals. *Genet. Med.* **25**, 90–102 (2023).
57. Yao, Z. *et al.* Preparation and evaluation of tetrabenazine enantiomers and all eight stereoisomers of dihydrotetrabenazine as VMAT2 inhibitors. *Eur J Med Chem* **46**, 1841–8 (2011).
58. Uhlyar, S. & Rey, J. A. Valbenazine (Ingrezza): The First FDA-Approved Treatment for Tardive Dyskinesia. *P T Peer-Rev. J. Formul. Manag.* **43**, 328–331 (2018).
59. Kremers, G.-J., Goedhart, J., Van Munster, E. B. & Gadella, T. W. J. Cyan and Yellow Super Fluorescent Proteins with Improved Brightness, Protein Folding, and FRET Förster Radius. *Biochemistry* **45**, 6570–6580 (2006).
60. Rothbauer, U. *et al.* A Versatile Nanotrap for Biochemical and Functional Studies with Fluorescent Fusion Proteins. *Mol. Cell. Proteomics* **7**, 282–289 (2008).
61. Reeves, P. J., Callewaert, N., Contreras, R. & Khorana, H. G. Structure and function in rhodopsin: High-level expression of rhodopsin with restricted and homogeneous N-glycosylation by a tetracycline-inducible *N*-acetylglucosaminyltransferase I-negative HEK293S stable mammalian cell line. *Proc. Natl. Acad. Sci.* **99**, 13419–13424 (2002).
62. Goehring, A. *et al.* Screening and large-scale expression of membrane proteins in mammalian cells for structural studies. *Nat Protoc* **9**, 2574–85 (2014).

63. Mastronarde, D. N. SerialEM: A Program for Automated Tilt Series Acquisition on Tecnai Microscopes Using Prediction of Specimen Position. *Microsc. Microanal.* **9**, 1182–1183 (2003).
64. Punjani, A., Rubinstein, J. L., Fleet, D. J. & Brubaker, M. A. cryoSPARC: algorithms for rapid unsupervised cryo-EM structure determination. *Nat Methods* **14**, 290–296 (2017).
65. Punjani, A., Zhang, H. & Fleet, D. J. Non-uniform refinement: adaptive regularization improves single-particle cryo-EM reconstruction. *Nat Methods* **17**, 1214–1221 (2020).
66. Scheres, S. H. RELION: implementation of a Bayesian approach to cryo-EM structure determination. *J Struct Biol* **180**, 519–30 (2012).
67. Sanchez-Garcia, R. *et al.* DeepEMhancer: a deep learning solution for cryo-EM volume post-processing. *Commun. Biol.* **4**, 874 (2021).
68. Jumper, J. *et al.* Highly accurate protein structure prediction with AlphaFold. *Nature* **596**, 583–589 (2021).
69. Wang, R. Y. *et al.* Automated structure refinement of macromolecular assemblies from cryo-EM maps using Rosetta. *Elife* **5**, (2016).
70. Emsley, P. & Cowtan, K. Coot: model-building tools for molecular graphics. *Acta Crystallogr. Biol. Crystallogr.* **60**, 2126–32 (2004).
71. Croll, T. I. *ISOLDE*: a physically realistic environment for model building into low-resolution electron-density maps. *Acta Crystallogr. Sect. Struct. Biol.* **74**, 519–530 (2018).
72. Liebschner, D. *et al.* Macromolecular structure determination using X-rays, neutrons and electrons: recent developments in Phenix. *Acta Crystallogr. Struct. Biol.* **75**, 861–877 (2019).
73. Green, E. M., Coleman, J. A. & Gouaux, E. Thermostabilization of the Human Serotonin Transporter in an Antidepressant-Bound Conformation. *PLoS One* **10**, e0145688 (2015).
74. Wu, E. L. *et al.* CHARMM-GUI *Membrane Builder* toward realistic biological membrane simulations. *J. Comput. Chem.* **35**, 1997–2004 (2014).

75. Lomize, M. A., Pogozheva, I. D., Joo, H., Mosberg, H. I. & Lomize, A. L. OPM database and PPM web server: resources for positioning of proteins in membranes. *Nucleic Acids Res.* **40**, D370–D376 (2012).
76. Olsson, M. H. M., Søndergaard, C. R., Rostkowski, M. & Jensen, J. H. PROPKA3: Consistent Treatment of Internal and Surface Residues in Empirical  $pK_a$  Predictions. *J. Chem. Theory Comput.* **7**, 525–537 (2011).
77. Phillips, J. C. *et al.* Scalable molecular dynamics with NAMD. *J. Comput. Chem.* **26**, 1781–1802 (2005).
78. Lee, J. *et al.* CHARMM-GUI Input Generator for NAMD, GROMACS, AMBER, OpenMM, and CHARMM/OpenMM Simulations Using the CHARMM36 Additive Force Field. *J. Chem. Theory Comput.* **12**, 405–413 (2016).
79. Klauda, J. B. *et al.* Update of the CHARMM All-Atom Additive Force Field for Lipids: Validation on Six Lipid Types. *J. Phys. Chem. B* **114**, 7830–7843 (2010).
80. Huang, J. *et al.* CHARMM36m: an improved force field for folded and intrinsically disordered proteins. *Nat. Methods* **14**, 71–73 (2017).
81. Vanommeslaeghe, K., Raman, E. P. & MacKerell, A. D. Automation of the CHARMM General Force Field (CGenFF) II: Assignment of Bonded Parameters and Partial Atomic Charges. *J. Chem. Inf. Model.* **52**, 3155–3168 (2012).
82. O'Boyle, N. M. *et al.* Open Babel: An open chemical toolbox. *J. Cheminformatics* **3**, 33 (2011).
83. Hoover, W. G. Canonical dynamics: Equilibrium phase-space distributions. *Phys. Rev. A* **31**, 1695–1697 (1985).
84. Nosé, S. A molecular dynamics method for simulations in the canonical ensemble. *Mol. Phys.* **52**, 255–268 (1984).
85. Essmann, U. *et al.* A smooth particle mesh Ewald method. *J. Chem. Phys.* **103**, 8577–8593 (1995).

86. Ryckaert, J.-P., Ciccotti, G. & Berendsen, H. J. C. Numerical integration of the cartesian equations of motion of a system with constraints: molecular dynamics of n-alkanes. *J. Comput. Phys.* **23**, 327–341 (1977).
87. Cheng, M. H., Kaya, C. & Bahar, I. Quantitative Assessment of the Energetics of Dopamine Translocation by Human Dopamine Transporter. *J. Phys. Chem. B* **122**, 5336–5346 (2018).
88. Chipot, C. & Hénin, J. Exploring the free-energy landscape of a short peptide using an average force. *J. Chem. Phys.* **123**, 244906 (2005).
89. Trott, O. & Olson, A. J. AutoDock Vina: Improving the speed and accuracy of docking with a new scoring function, efficient optimization, and multithreading. *J. Comput. Chem.* NA-NA (2009) doi:10.1002/jcc.21334.
90. Cheng, M. H. *et al.* Insights into the Modulation of Dopamine Transporter Function by Amphetamine, Orphenadrine, and Cocaine Binding. *Front. Neurol.* **6**, (2015).
91. Yang, D. & Gouaux, E. Illumination of serotonin transporter mechanism and role of the allosteric site. *Sci Adv* **7**, eabl3857 (2021).
92. Humphrey, W., Dalke, A. & Schulten, K. VMD: Visual molecular dynamics. *J. Mol. Graph.* **14**, 33–38 (1996).
93. Vangone, A. *et al.* Large-scale prediction of binding affinity in protein–small ligand complexes: the PRODIGY-LIG web server. *Bioinformatics* **35**, 1585–1587 (2019).
94. Kaynak, B. T., Bahar, I. & Doruker, P. Essential site scanning analysis: A new approach for detecting sites that modulate the dispersion of protein global motions. *Comput. Struct. Biotechnol. J.* **18**, 1577–1586 (2020).
95. Le Guilloux, V., Schmidtke, P. & Tuffery, P. Fpocket: An open source platform for ligand pocket detection. *BMC Bioinformatics* **10**, 168 (2009).
96. Zhang, S. *et al.* ProDy 2.0: increased scale and scope after 10 years of protein dynamics modelling with Python. *Bioinformatics* **37**, 3657–3659 (2021).

97. Yariv, B. *et al.* Using evolutionary data to make sense of macromolecules with a “face-lifted” ConSurf. *Protein Sci.* **32**, (2023).
98. Pei, J., Kim, B.-H. & Grishin, N. V. PROMALS3D: a tool for multiple protein sequence and structure alignments. *Nucleic Acids Res.* **36**, 2295–2300 (2008).
99. Schrödinger Release 2023-4: Maestro, Schrödinger, LLC, New York, NY, 2023.

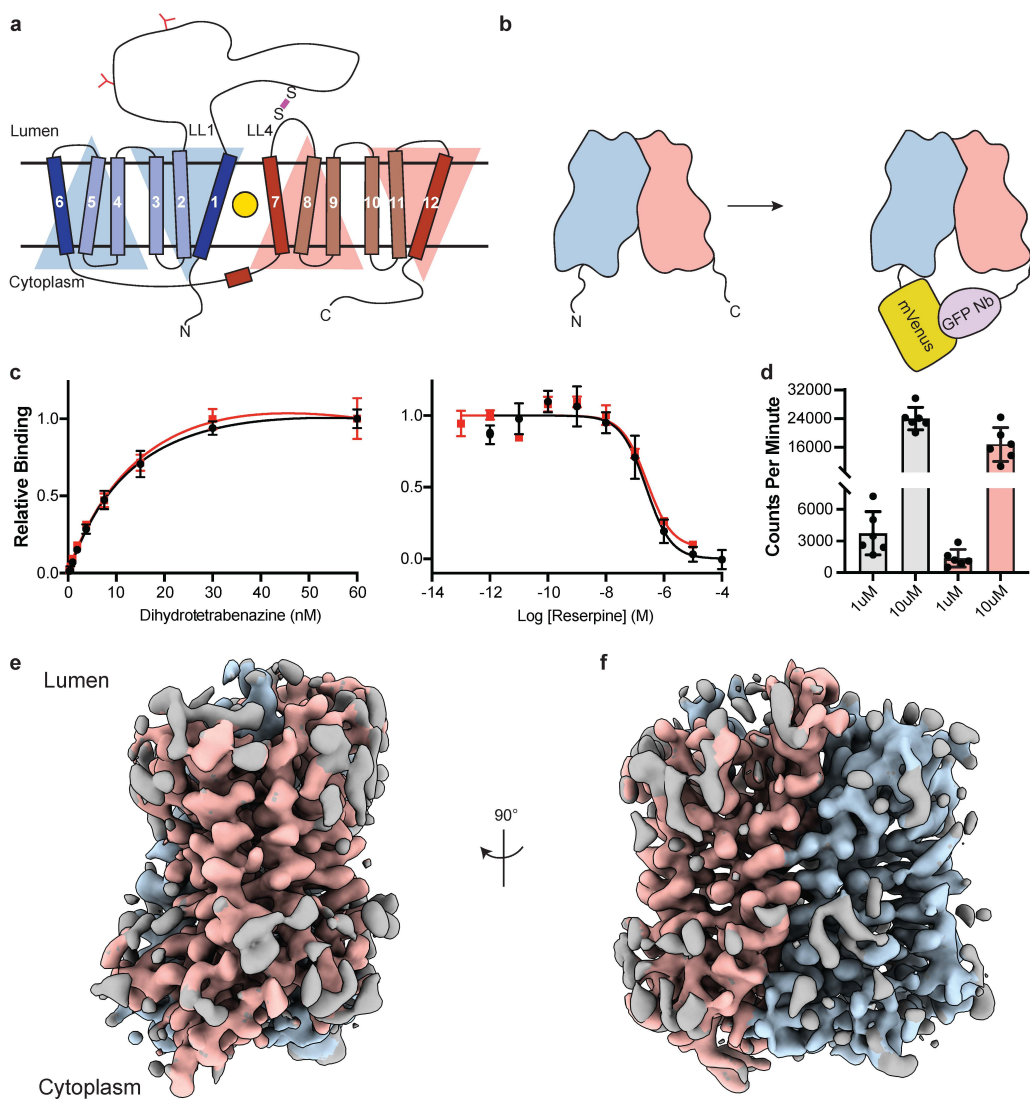


Figure 1

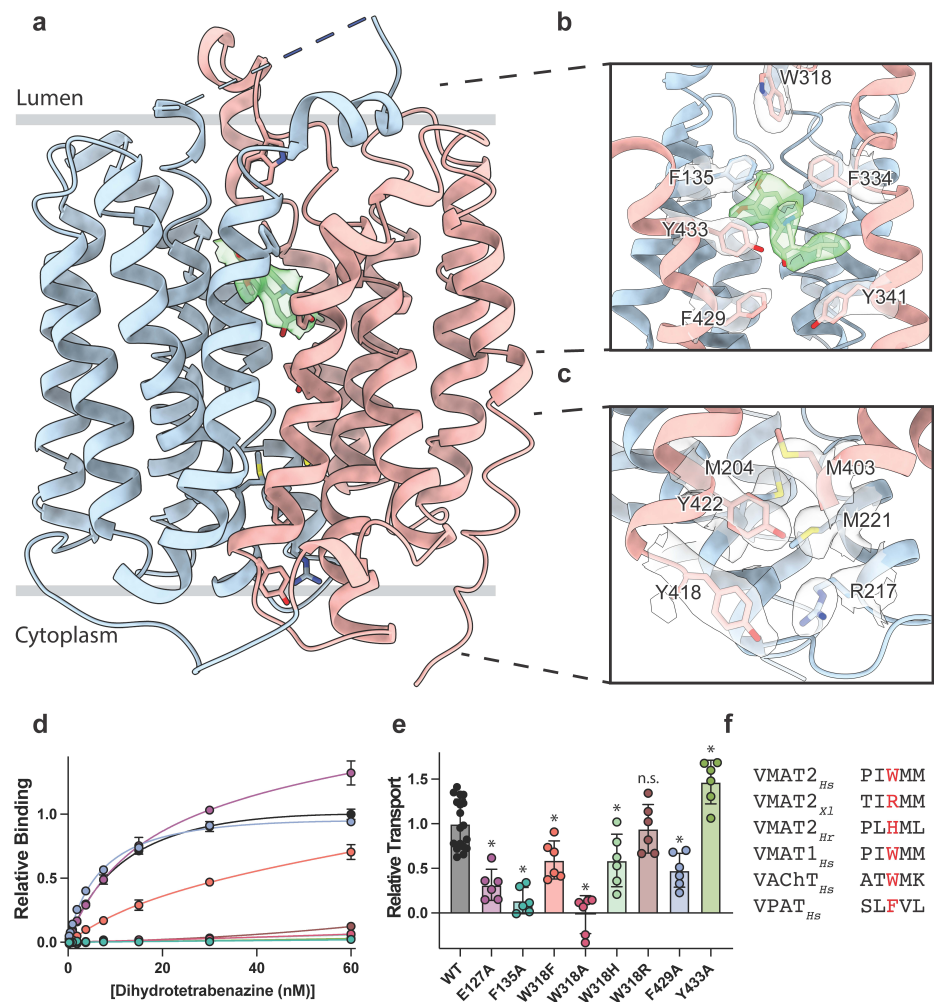


Figure 2

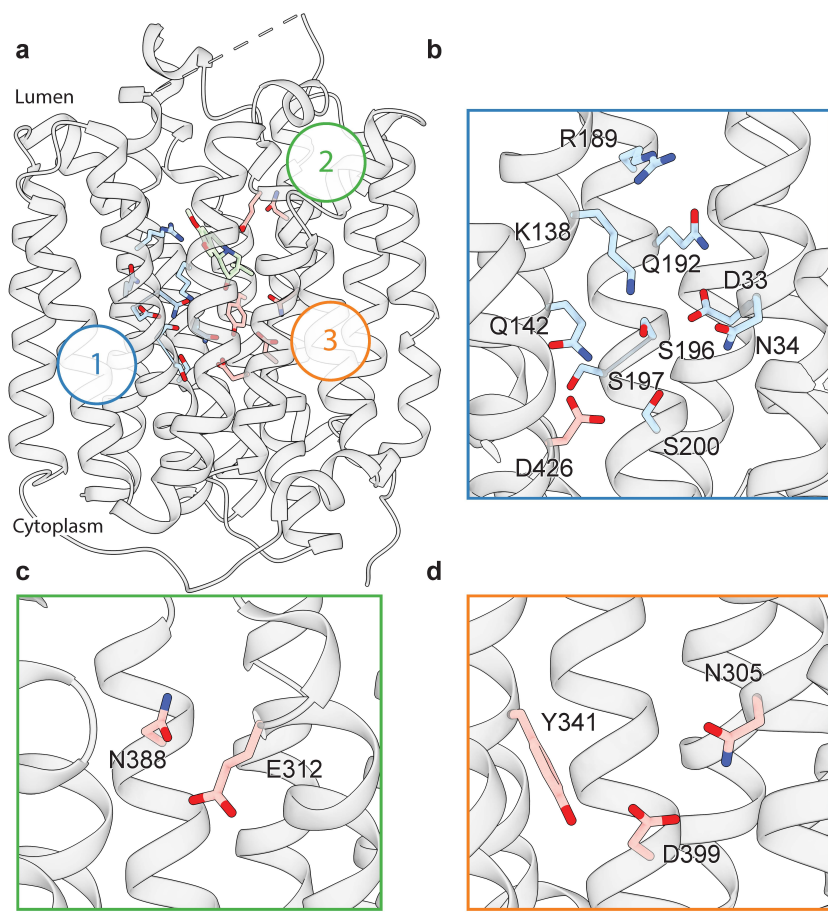


Figure 3

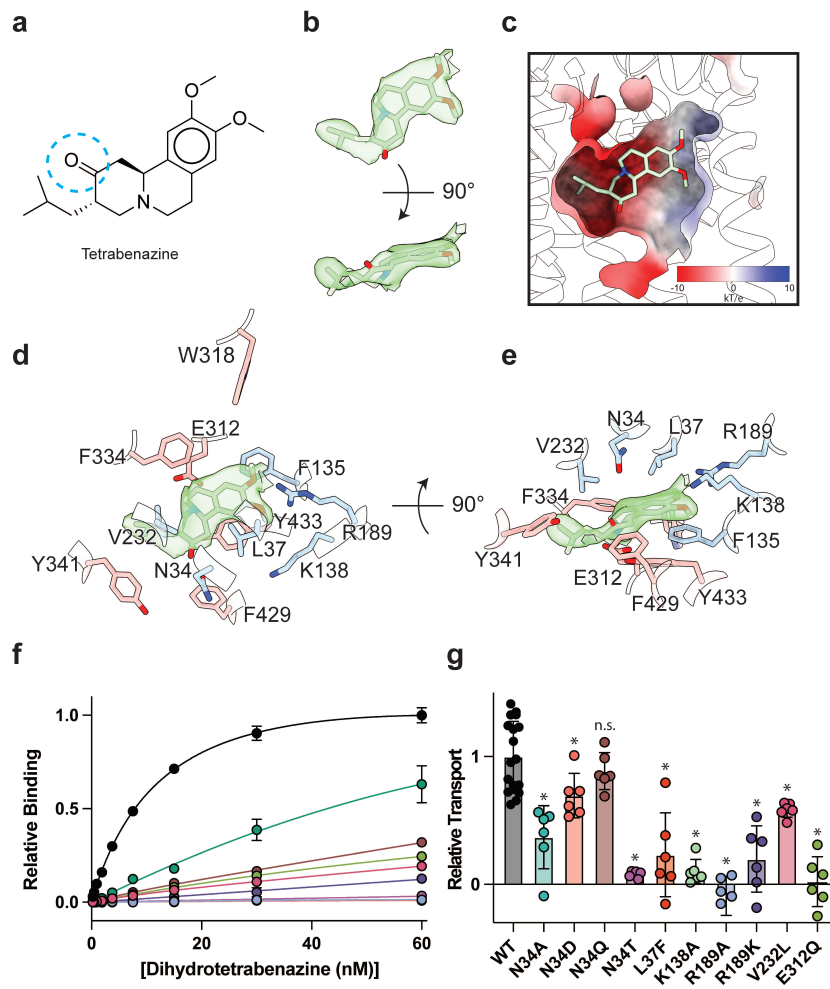


Figure 4

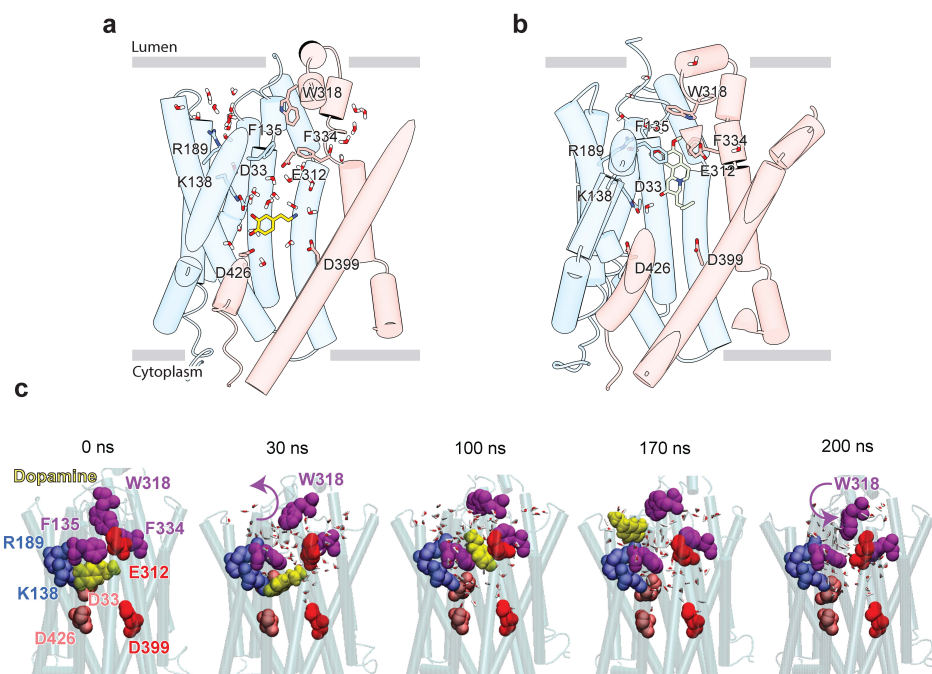


Figure 5

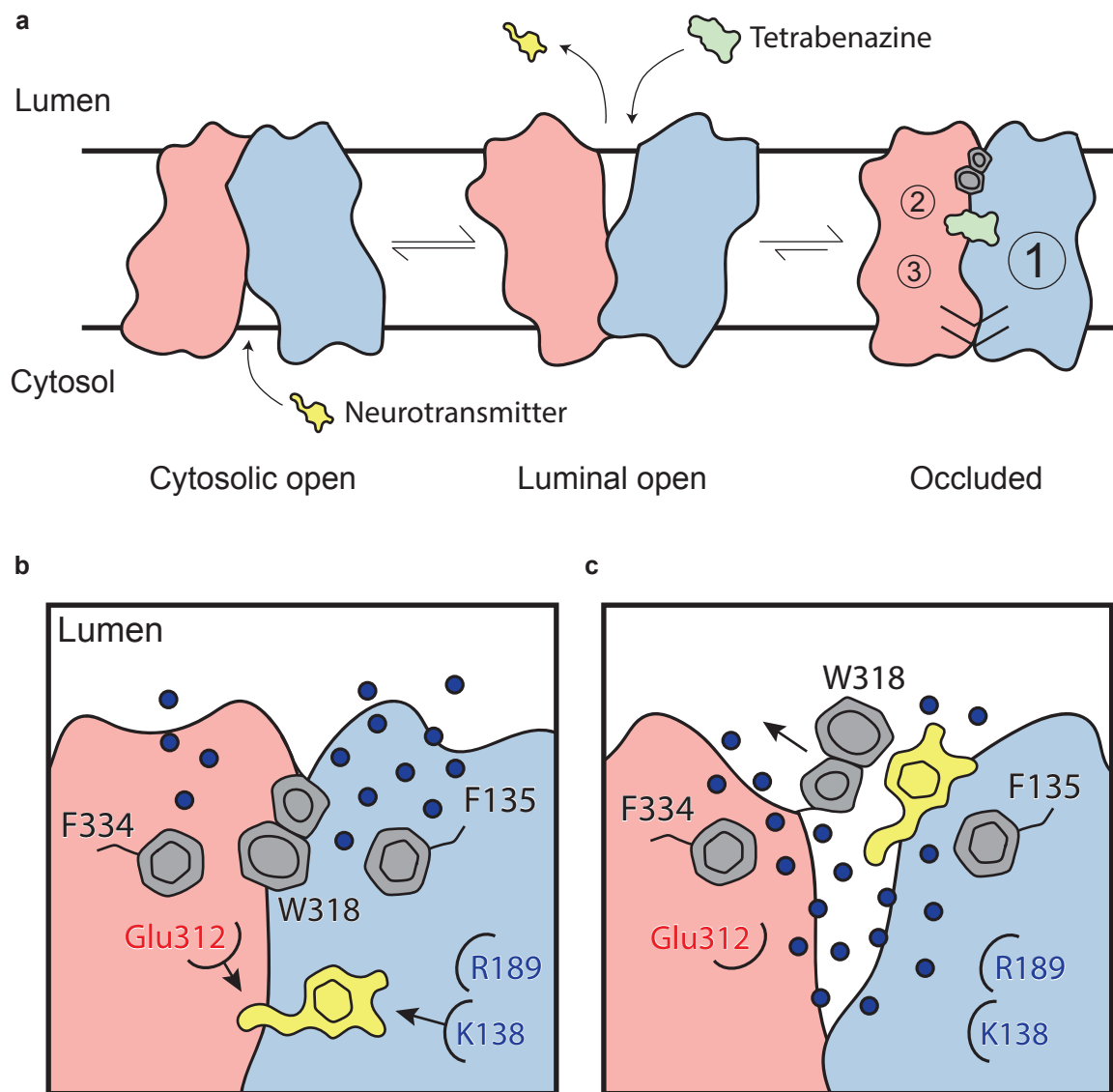


Figure 6